Draft version February 6, 2017
Preprint typeset using LaTeX style AASTeX6 v. 1.0

arXiv:1702.00803v1 [astro-ph.SR] 2 Feb 2017

TESTING METAL POOR STELLAR MODELS AND ISOCHRONES WITH HST PARALLAXES OF METAL POOR STARS

B. Chaboyer[1,2], B.E. McArthur[3], E. O'Malley[1], G.F. Benedict[3], G. A.Feiden[4], T.E. Harrison[5], A. McWilliam[6], E.P. Nelan[7], R.J. Patterson[8], A. Sarajedini[9]

[1]Dept. of Physics and Astronomy, Dartmouth College, Hanover, NH 03755 USA
[2]Max-Planck-Institut für Astrophysik, Karl-Schwarzschild-Str. 1, D-85748 Garching bei München, Germany
[3]McDonald Observatory, University of Texas, Austin, TX 78712 USA
[4]Department of Physics and Astronomy, Uppsala University, Box 516, SE-751 20, Uppsala, Sweden
[5]Dept. of Astronomy, New Mexico State University, Las Cruces, NM 88003 USA
[6]The Observatories of the Carnegie Institute of Washington, Pasadena, CA 91101 USA
[7]Space Telescope Science Institute, Baltimore, MD 21218 USA
[8]Dept. of Astronomy, University of Virginia, Charlottesville, VA 22904 USA
[9]Dept. of Astronomy, University of Florida, Gainesville, FL 32611 USA

ABSTRACT

Hubble Space Telescope (HST) fine guidance sensor observations were used to obtain parallaxes of eight metal-poor ([Fe/H] < -1.4) stars. The parallaxes of these stars determined by the new *Hipparcos* reduction average 17% accuracy, in contrast to our new *HST* parallaxes which average 1% accuracy and have errors on the individual parallaxes ranging from 85 to 144 *microarcseconds*. This parallax data has been combined with HST ACS photometry in the F606W and F814W filters to obtain the absolute magnitudes of the stars with an accuracy of 0.02 to 0.03 magnitudes. Six of these stars are on the main sequence (with $-2.7 <$ [Fe/H] < -1.8), and suitable for testing metal-poor stellar evolution models and determining the distances to metal-poor globular clusters. Using the abundances obtained by O'Malley et al. (2016) we find that standard stellar models using the VandenBerg & Clem (2003) color transformation do a reasonable job of matching five of the main sequence stars, with HD 54639 ([Fe/H] $= -2.5$) being anomalous in its location in the color-magnitude diagram. Stellar models and isochrones were generated using a Monte Carlo analysis to take into account uncertainties in the models. Isochrones which fit the parallax stars were used to determine the distances and ages of nine globular clusters (with $-2.4 \leq$ [Fe/H] ≤ -1.9). Averaging together the age of all nine clusters, leads to an absolute age of the oldest, most metal-poor globular clusters of 12.7 ± 1.0 Gyr, where the quoted uncertainty takes into account the known uncertainties in the stellar models and isochrones, along with the uncertainty in the distance and reddening of the clusters.

Keywords: stars: Population II, stars: distances, astrometry, globular clusters

1. INTRODUCTION

Stellar evolution models and isochrones are widely used in astrophysics to determine the properties of stars and integrated stellar populations. The predicted absolute magnitudes and colors of stars are frequently used, yet there are few tests of these basic properties of stellar models and isochrones for metal-poor stars. Stars on the main sequence provide a stringent test of stellar evolution models, as their properties vary little with age. In contrast, the properties of more evolved stars are sensitive to the age of the star, and stellar evolution models are typically assumed to be correct and used to determine the ages of stars which have evolved off the main sequence. To test metal-poor stellar models and isochrones, it is important to have high quality absolute magnitudes and colors of single, main sequence stars.

The *Hipparcos* catalog (Perryman & ESA 1997; van Leeuwen 2007) provided accurate parallaxes for a large number of stars and was used to investigate a large number of issues in stellar astrophysics, including the distances and ages of globular clusters (e.g. Reid 1997; Gratton et al. 1997; Pont et al. 1998; Chaboyer et al. 1998; Carretta et al. 2000; Grundahl et al. 2002; Gratton et al. 2003). One of the key limitations of the *Hipparcos* catalog for studying metal-

poor stars is that it only contained one single main sequence star with [Fe/H] < -1.5 whose parallax was known to a sufficient accuracy ($\sim 10\%$) to provide a reasonable test of stellar models. To investigate the reliability of low metallicity stellar models prior to the *Gaia* data release, and to illustrate the types of studies enabled by high quality parallaxes, we have obtained HST fine guidance sensor (FGS) observations of nine metal-poor stars, and parallaxes of eight of these stars are presented in this paper. The HST observations started on Oct. 28, 2008 and were completed on June 3, 2013. In addition to illustrating the type of science possible with high quality parallaxes of metal-poor stars, this work provides accurate parallaxes which can be used to cross-check the Tycho-*Gaia* astrometric solution (TGAS) (Michalik, Lindegren & Hobbs 2015; Gaia Collaboration et al. 2016; Lindegren et al. 2016), which was released after this paper was submitted for publication. The uncertainties in our parallaxes range from 85 to 144 μas, which are lower than the TGAS parallax uncertainties, which range from 220 to 860 μas for our target stars (Lindegren et al. 2016).

The stars selected for HST observations were selected from various lists of metal-poor stars. The key criteria used to select stars for the HST observations were (a) estimated [Fe/H] < -1.5, (b) the star was not a known member of a multiple star system, and (c) that the star be on the main sequence. To determine if a star was on the main sequence, we selected stars which were relatively cool ($V - I > 0.7$) and which had high surface gravities (based upon estimates from high-resolution spectroscopy, or Stömgren photometry).

Details of our observations and data reductions are presented in §2. The derived parallaxes are discussed in §3, where we determine that two of the stars are in the main-sequence turn-off or sub-giant branch phase of evolution and so are not useful for testing stellar models. These two stars turned out to suffer from significant reddening and as a result were bluer than was assumed during our sample selection. The main sequence stars are compared to stellar isochrones in §4, and the isochrones which fit these calibrating stars are used to derive distances and ages of a number of metal-poor globular clusters in §5. Our key results are summarized in §6.

2. OBSERVATIONS

2.1. *HST Photometry of Program Stars*

In order to compare the magnitudes of our program stars with HST color-magnitude diagrams of globular clusters, each program star was observed with ACS/WFC in the F606W and F814W filters. The CTE-corrected ACS/WFC images for the program stars were retrieved from MAST. Each of them was multiplied by the geometric correction image, and the image quality file was applied in order to mask-out pixels of lower quality. Photometry with a 0.5 arcsec aperture was performed on the program stars in the resultant images. These instrumental magnitudes were corrected for exposure time, matched to form colors, and calibrated to the VEGAMag and ground-based VI systems using the Sirianni et al. (2005) photometric transformations. Ground based photometry for all of our program stars were obtained using the NMSU 1 m telescope, the MDM 1.3m telescope and the SMARTS 0.9 m telescope. Further details are provided in §A.1.

A summary of HST and ground based photometry of the program stars is presented in Table 1. For each star, we list our own ground based measurements, along with photoelectric photometer observations from the literature. For several stars, there is a considerable range in the V and $V - I$ measurements. We recommend averaging the V and $V - I$ measurements to obtain the best estimate of the apparent magnitude and color of each star. Given the scatter in the data, an uncertainty of 0.01 mag in the observed V magnitudes and $V - I$ colors of the stars seems appropriate.

Table 1. Photometry of Program Stars

ID	Telescope	V	$V - I$	F606W	F606W — F814W
HIP 46120	HST	10.097	0.752	9.938 ± 0.0015	0.566 ± 0.0023
	SSO[a]	10.15	0.725	···	···
HIP 54639	HST	11.354	0.917	11.149 ± 0.0017	0.688 ± 0.0044
	MDM	11.377	0.911	···	···
	KPNO[b]	11.40	···	···	···
HIP 56291[c]	HST	11.519	0.865	11.328 ± 0.0024	0.649 ± 0.0069
	MDM	11.575	0.845	···	···
	KPNO[b]	11.53	···	···	···

Table 1 continued on next page

Table 1 *(continued)*

ID	Telescope	V	$V-I$	F606W	F606W — F814W
HIP 87062	HST	10.565	0.848	10.379 ± 0.0003	0.636 ± 0.0021
	NMSU	10.57	0.83	···	···
	MDM	10.56	0.82	···	···
	KPNO[d]	10.60	···	···	···
HIP 87788	HST	11.298	0.856	11.109 ± 0.0031	0.642 ± 0.0034
	NMSU	11.33	0.87	···	···
	MDM	11.29	0.83	···	···
	KPNO[d]	11.29	···	···	···
HIP 98492	HST	11.559	0.832	11.377 ± 0.0051	0.625 ± 0.0055
	NMSU	11.58	0.80	···	···
	MDM	11.57	0.80	···	···
	KPNO[b]	11.59	···	···	···
	OAN-SPM[e]	11.568	···	···	···
HIP 103269	HST	10.249	0.772	10.084 ± 0.0034	0.581 ± 0.0043
	NMSU	10.28	0.79	···	···
	MDM	10.29	0.75	···	···
	KPNO[b]	10.27	···	···	···
HIP 106924	HST	10.328	0.799	10.156 ± 0.0024	0.601 ± 0.0054
	NMSU	10.42	0.87	···	···
	MDM	10.36	0.74	···	···
	KPNO[b]	10.34	···	···	···
HIP 108200	HST	10.974	0.856	10.785 ± 0.0031	0.643 ± 0.0063
	NMSU	10.97	0.83	···	···
	MDM	11.00	0.82	···	···
	KPNO[d]	11.03	···	···	···

[a] Bessel, M.S. 1990 (Cousins (Kron-Cape) system)

[b] Carney & Latham 1987

[c] Missing FGS parallax

[d] Carney *et al.* 1994

[e] Silva, Schuster & Contreras 2012

2.2. *HST Astrometry Observations*

We used *HST* FGS-1r, a two-axis interferometer, in position (POS) "fringe-tracking" mode[1] to make the astrometric observations. Nelan (2007) describes the FGS instrument. The reduction and calibration of the data is described in Benedict et al. (2007). A new improved Optical Field Angle Distortion (OFAD) derived by McArthur, was used to reduce and calibrate the data which is available with the reduction pipeline. This astrometric data are available from the HST Program Schedule and Information website, in proposal numbers 11704 and 12320. Eighty-nine orbits of *HST* astrometric observations were made between December 2008 and June 2013. Every orbit contains several observations of the target and surrounding reference stars. The latest calibrations parameters and the two part pipeline used to reduce the raw data to the values used in this modeling is available from the Space Telescope Science Institute in IRAF STSDAS and in a standalone version available from one of the coauthors, the *HST* FGS Instrument Scientist at STSCI Ed Nelan.

With respect to its reference frame, an *HST* target parallax is relative, not absolute. For a conversion from a relative to and absolute frame, we can use a statistically- derived correction (c.f. van Altena et al. 1995), or we can use the derived spectroscopic parallaxes of the reference frame stars as input to the model in a Bayesian approach. For

[1] A detailed Instrument Handbook can be found on the Space Telescope Science Institute website.

finer accuracy, we use the Bayesian approach, in which we estimate the absolute parallaxes of the reference frame stars using spectra to classify the temperature and luminosity class of each star, and then combine these with $UBVRIJHK$ photometry to determine their visual extinctions, as described in Harrison et al. (2013). We require the absolute magnitude, M_V, and V-band absorption, A_V for the equation

$$\pi_{\rm abs} = 10^{-(V-M_V+5-A_V)/5} \tag{1}$$

Our modeling then produces not a relative parallax, but an absolute parallax.

Full details of our astrometric reductions are provided in the Appendix. Below, we summarize the key details. Each reference frame contained from 5 to 9 reference stars plus the target. The positions (x', y') of the target and reference stars change with each observation set because *HST* rolls with the observations shown in Table A1. We use parameters for scale, rotation, and offset in an overlapping plate model. We relate each plate's parameters to a master constrained plate, usually one of the central observations. The astrometric model also includes the time-dependent movements of each star, given by the absolute parallax π_{abs} and the proper motion components, μ_α and μ_δ, which are transformed into the roll of the constraint plate. We also include instrumentally caused position shift parameters for lateral color. The standard coordinate catalog positions ξ and η are the result of modeling these equations of condition:

$$x' = x + lc_x(B-V) - \Delta XFx \tag{2}$$
$$y' = y + lc_x(B-V) - \Delta XFy \tag{3}$$

$$\xi = Ax' + By' + C - \mu_\xi \Delta t - P_\xi \pi \tag{4}$$
$$\eta = Dx' + Ey' + F - \mu_\eta \Delta t - P_\eta \pi \tag{5}$$

where x and y are the measured coordinates from *HST*; lc_x and lc_y are the lateral color corrections, and $B-V$ are the $B-V$ colors of each star. A, B, D, and E, are scale and rotation plate constants, and C and F are offsets. The constraint plate defines A and E equal to 1, B and D equal to 0, and C and F equal to 0. μ_ξ and μ_η are proper motions, Δt is the epoch difference from the mean epoch, P_ξ and P_η are parallax factors, and π is the parallax. We get the parallax factors from a JPL Earth orbit predictor (Standish 1990, upgraded to version DE405). We use a model in the GaussFit language (Jefferys et al. 1988) utilizing robust estimation to derive a simultaneous solution for all parameters. The resulting astrometric catalogs from the combined modeling are shown in Table A8.

Condition equations relate an initial and final parameter value. All input data supplied to the equations of condition (such as reference star proper motions from catalogs and spectrophotometric parallaxes) are input to the model with errors. The lateral color term of all stars and the *HST* roll reported by the spacecraft of the constraint plate are also input with their errors in additional equations of condition. These additional equations of condition allow the χ^2 minimization process to adjust parameter values by amounts constrained by their input errors. In this quasi-Bayesian approach, prior knowledge is not input as a hardwired quantity known to infinite precision, but input as an observation with associated error. For all metal-poor target (not reference) stars no priors were used for parallax or proper motion.

3. *HST* PARALLAX AND PROPER MOTIONS OF THE TARGET STARS

The parallaxes of the metal-poor target stars are shown in Table 2, including independently determined values from the updated *Hipparcos* catalogue (van Leeuwen 2007) for comparison. Our determination yielded uncertainties between 85 and 144 micro-arseconds, with an average uncertainty of 1% on the parallax, a very high accuracy. In contrast, the new *Hipparcos* reduction yielded uncertainties of 17%, while the recently released TGAS parallaxes typically have uncertainties a factor of two larger than the HST uncertainties. The proper motions shown in Table 3 agree with *Hipparcos* and URAT1 values, with *HST* motions having smaller uncertainties. *HST* proper motions are relative to the reference frame. No a priori values for proper motion and parallax were used as input for the target stars, only for the reference frame.

Table 2. Metal-Poor Target Star Parallaxes

HIP ID	HST (mas)	HIP07 (mas)	TGAS17 (mas)
46120	15.011 ± 0.119	15.2 ± 0.98	14.938 ± 0.211

Table 2 continued on next page

Table 2 *(continued)*

HIP ID	HST (mas)	HIP07 (mas)	TGAS17 (mas)
54639	11.116 ± 0.113	15.69± 2.79	12.258 ± 0.232
87062	8.205 ± 0.110	9.59 ± 2.21	8.383 ± 0.860
87788	10.830 ± 0.127	10.01± 2.79	10.972 ± 0.258
98492	3.487 ± 0.144	9.78 ± 2.77	2.484 ± 0.371
103269	14.118 ± 0.099	14.86± 1.31	13.760 ± 0.220
106924	14.474 ± 0.100	15.11± 1.26	···
108200	12.397 ± 0.085	12.33± 1.76	···

Table 3. Metal-Poor Target Star Proper Motions

ID	HST μ_{RA}	HSTμ_{DEC}	HIP μ_{RA}	HIPμ_{DEC}	PPMXL cat μ_{RA}	PPMXL catμ_{DEC}
46120	203.410±0.116	1236.325±0.123	202.17±1.13	1236.93±1	202.1±1	1237.2±1
54639	-567.057± 0.111	-517.165± 0.101	-567.16±3.62	-509.01±2.06	568.5±2.2	517.7±2.1
87062	244.342 ±0.079	-366.504±0.088	242.57±2.29	-364.62±1.4	244.8±1.6	-365.3±1.2
87788	5.88±0.078	-625.569± 0.088	6.67 ± 2.85	-626.66±1.88	-0.6± 8.7	-629.1±5.6
98492	-186.256± 0.111	-186.256±0.115	-195.17±3.27	-194.57±2.61	-186.6±6.2	-185.9± 6.2
103269	57.749±0.111	-389.392±0.117	57.62±1.24	-390.72±1.24	55.9 ±1.1	-391±1
106924	-382.527± 0.092	232.585±0.106	-381.67±1.14	232.74±1.13	-381.6±1.1	232.7±1
108200	760.661±0.092	127.455±0.099	762.57±1.19	132.16±1.96	761.6±1.3	128.5±2

The key properties of our target stars are summarized in Table 4. High resolution spectroscopic abundances and reddening estimates are from O'Malley et al. (submitted). The reddening estimates are based upon the strength of the interstellar Na I line in the high resolution spectra of the target stars. If no interstellar Na I lines were detected, then the reddening was estimated to be less than 0.001 mag, and was assumed to be zero for that star. For stars with non-zero reddening, an uncertainty of 10% in the reddening was added in quadrature with the uncertainty in the parallax to determine the uncertainty in the absolute magnitudes. No Lutz & Kelker (1973) corrections have been applied to Table 4 as the high accuracy of the parallaxes make these corrections negligible (less than 0.0008 mag). The stars are plotted in an color-absolute magnitude diagram in Figure 1. Below we briefly comment on each of the target stars.

Table 4. Summary of Parallax Star Properties

ID	V	V – I	E(B – V)	$(V\text{-}I)_o$	M_V	M_{F606W}[a]	[Fe/H]	[α/Fe][b]
46120	10.12	0.752	0.00	0.738	6.00 ± 0.02	5.81	−2.22	0.29
54639	11.38	0.914	0.00	0.914	6.61 ± 0.02	6.37	−2.50	0.19
87062	10.57	0.833	0.06	0.750	4.95 ± 0.03	4.77	−1.56	0.1
87788	11.30	0.852	0.00	0.852	6.47 ± 0.03	6.27	−2.66	0.61
98492	11.57	0.811	0.11	0.659	3.94 ± 0.09	3.78	−1.40	0.4
103269	10.27	0.771	0.00	0.771	6.02 ± 0.02	5.83	−1.83	0.06
106924	10.36	0.803	0.00	0.803	6.16 ± 0.02	5.95	−2.23	0.23
108200	10.99	0.835	0.02	0.807	6.40 ± 0.01	6.19	−1.83	0.01

[a] Uncertainty the same as the M_V values.

[b] Based upon the abundance of calcium, an α-capture element.

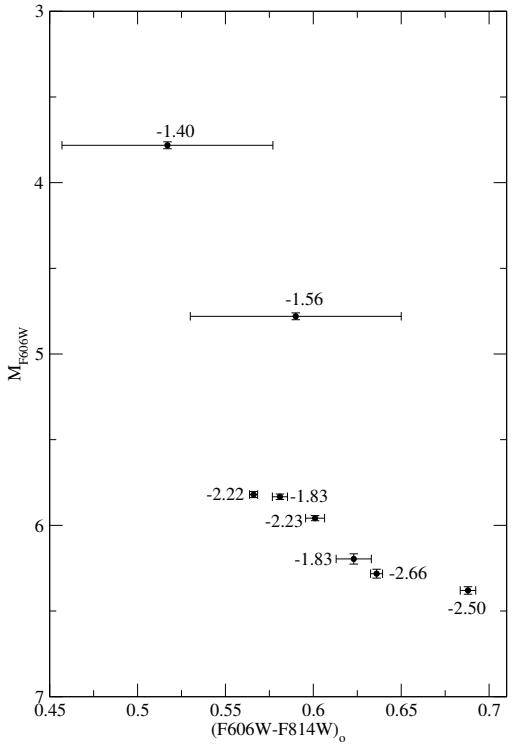

Figure 1. The location of the stars in the color-absolute magnitude diagram. Each star is labeled with its [Fe/H] value (see Table 4).

HIP 46120 is typical main sequence star, with [Fe/H] = −2.24 and will serve as an excellent calibrator of the main sequence for the most metal-poor globular clusters. The *HST*, *Hipparcos* and TGAS parallaxes agree with each other for this star.

HIP 54639 is the reddest (and intrinsically faintest) star in the sample. This star has [Fe/H] = -2.5, and isochrones would prefer that this star be fainter by about 0.2 mag. The *HST* and TGAS parallaxes agree with each other, while the *Hipparcos* parallaxe agrees at the $1.6\,\sigma$ level for this star. The *Hipparcos* parallax of 15.679 mas (this is a faint star for *Hipparcos* with high error) would make this star fainter by 0.7 mag, the *HST* parallax of 11.116 mas has the star closer to the theoretical isochrone than the *Hipparcos* value.

Initial observations of HIP 56291 had *HST* target acquisition failures. The first was because of incorrect target position and that was corrected, but then there were star acquisition failures, most likely because the reference stars in this field were all fainter than the catalogs indicated. New reference stars were chosen, but some proved to be double stars, which locked on to different components. It may be possible to recover enough data to get a parallax, but it would be of significantly lower quality and as a result, a parallax was not determined for this star.

The *HST*, TGAS and *Hipparcos* parallaxes for HIP 87062 are in agreement. High resolution spectra show the presence of interstellar Na I lines (O'Malley et al. submitted) indicating that this star has $E(B-V) = 0.06$ magnitudes. As a result, the star is bluer than indicated by its colors, and the *HST* parallax indicate that the star is in the main sequence turn-off, region (with $M_v = 4.95$) and hence not suitable to use for main sequence fitting, or to test the stellar evolution isochrones. The location of this star in a color-magnitude diagram differs considerably from the other stars, and from theoretical isochrones. This suggests that we have may be using an incorrect reddening for this star. The Strömgren photometry from Schuster et al. (2006) implies $E(B-V) = 0.12$ suggesting that our reddening value could be in error. Using this reddening value puts the star's location in the color-magnitude diagram in better agreement with other stars.

HIP 87788 is the most metal-poor star in our sample, with [Fe/H] = −2.69. The *HST*, TGAS and *Hipparcos* parallaxes agree. This star is on the main sequence, and with no known reddening and an accurate parallax HIP 87788 is an excellent calibrator for the lowest metallicity stellar stellar models.

The parallax of the faintest star in our sample, HIP 98492 is discrepant at the $2.2\,\sigma$ level between *HST* (3.49 mas) and *Hipparcos* (9.78 mas). This star is very faint for *Hipparcos*. The TGAS parallax (2.48 mas) is much closer to the HST value, but formally, the TGAS and HST parallaxes disagree $2.5\,\sigma$ level. We note that Stassun & Torres

(2016) have found that the TGAS parallaxes are too small by 0.25 mas (when compared to eclipsing binaries), and offsetting the TGAS parallax by this amount would reduce the discrepancy with the HST parallax to $1.9\,\sigma$. High resolution spectra show the presence of interstellar Na I lines (O'Malley et al. submitted) indicating that this star has $E(B-V) = 0.11$ magnitudes. Silva et al. (2012) obtained Strömgren photometry of this star and also estimate $E(B-V) = 0.11$. This star is in the main sequence turn-off or sub-giant branch region. As a result, it is not suitable for testing stellar evolution models. Its location in the color-magnitude diagram is somewhat anomalous, which could be due to an incorrect reddening estimate.

HIP 103269 is a relatively metal-rich main sequence star in our sample, with [Fe/H] = −1.85. The *HST* and *Hipparcos* parallaxes agree at the $0.6\,\sigma$ level for this star and place it on the main sequence. The TGAS parallax agrees at the $1.5\,\sigma$ level with the HST parallax. Offsetting the TGAS parallax by 0.25 mas, brings the TGAS and HST parallax into agreement at the $0.4\,\sigma$ level. With no reddening, and a well determined absolute magnitude, HIP 103269 is another excellent calibrator for low metallicity stellar models.

HIP 106924 is a typical main sequence star, with [Fe/H] = −2.22 and will serve as an excellent calibrator of the main sequence for the most metal-poor globular clusters. The *HST* and *Hipparcos* parallaxes agree with each other at the $0.5\,\sigma$ level for this star. This star is not in the TGAS catalogue.

HIP 108200 is another relatively metal-rich main sequence star in our sample (with [Fe/H] = −1.83). It has a small reddening of $E(B-V) = 0.02$ mag based upon the interstellar Na I lines (O'Malley et al. submitted).The *HST* and *Hipparcos* parallaxes agree at the $0.6\,\sigma$ level for this star and place it on the main sequence. With a small reddening, and a well determined absolute magnitude, HIP 108200 is another good calibrator for low metallicity stellar models. This star is not in the TGAS catalogue.

4. COMPARISON TO THEORETICAL ISOCHRONES

The reliability of theoretical stellar models and isochrones is tested by comparison of these stars in color and magnitude to the Dartmouth isochrones (Dotter et al. 2008). The theoretical uncertainty in stellar evolution models is estimated by constructing 2000 independent isochrones via a Monte Carlo analysis similar to Bjork & Chaboyer (2006). This Monte Carlo analysis uses probability distributions for the various input parameters which have intrinsic uncertainties associated with their value. For example, a comparison between different opacity calculations suggests that current high temperature ($T \geq 10^7$ K) opacities are uncertain at the 3% level and so when constructing the stellar models, the tabulated opacities are multiplied by a number randomly drawn from a Gaussian distribution with a mean of 1, and $\sigma = 0.03$. The probability density distributions of the stellar evolution parameters varied in the Monte Carlo simulation are provided in Table 5. Starting with the probability density distributions used by Bjork & Chaboyer (2006), we updated the nuclear reaction rates, helium abundance, and choice of model atmosphere to reflect more recent measurements/calculations. References for our choice of parameter distributions are given in Table 5 and our choice of the mixing length distribution merits further discussion.

Table 5. Monte Carlo Stellar Evolution Parameter Density Distributions

Parameter	Distribution	Standard	Type
He mass fraction (Y) .	0.24725 - 0.24757	Planck Collaboration XVI (2014)	Uniform
Mixing length	1.00 - 1.70	N/A	Uniform
Convective overshoot .	$0.0H_p$ - $0.2H_p$	N/A	Uniform
Atmospheric $T(\tau)$	33.3/33.3/33.3	Eddington (1926) or Krishna Swamy (1966), or Hauschildt et al. (1999)	Triinary
Low-T opacities	0.7 - 1.3	Ferguson et al. (2005)	Uniform
High-T opacities.....	1.00% ± 3% ($T \geq 10^7$ K)	Iglesias & Rogers (1996)	Gaussian
Diffusion coefficients..	0.5 - 1.3	Thoul et al. (1994)	Uniform
$p + p \rightarrow {}^2\mathrm{H} + e^+ + \nu_e$	1% ± 1%	Adelberger et al. (2011)	Gaussian
${}^3\mathrm{He} + {}^3\mathrm{He} \rightarrow {}^4\mathrm{He} + 2p$	1% ± 5%	Adelberger et al. (2011)	Gaussian
${}^3\mathrm{He} + {}^4\mathrm{He} \rightarrow {}^7\mathrm{Be} + \gamma$.	1% ± 2%	deBoer et al. (2014)	Gaussian
${}^{12}\mathrm{C} + p \rightarrow {}^{13}\mathrm{N} + \gamma$ ...	1% ± 36%	Xu et al. (2013)	Gaussian
${}^{13}\mathrm{C} + p \rightarrow {}^{14}\mathrm{N} + \gamma$ ...	1% ± 15%	Chakraborty et al. (2015)	Gaussian

Table 5 continued on next page

Table 5 *(continued)*

Parameter	Distribution	Standard	Type
$^{14}N + p \rightarrow ^{15}O + \gamma \ldots$	1% ± 7%	Adelberger et al. (2011)	Gaussian
$^{16}O + p \rightarrow ^{17}F + \gamma \ldots$	1% ± 16%	Adelberger et al. (1998)	Gaussian
Triple-α reaction rate.	1% ± 15%	Angulo et al. (1999)	Gaussian
Neutrino cooling rate.	1% ± 5%	Haft et al. (1994)	Gaussian
Conductive opacities..	1% ± 20%	Hubbard & Lampe (1969) plus Canuto (1970)	Gaussian

NOTE—As in Bjork & Chaboyer (2006), parameters below Atmospheric $T(\tau)$ are treated as multiplicative factors applied to standard tables and formulas.

The stellar models use a mixing length prescription to describe convection. This theory has two free parameters (the mixing length itself, α, and the degree of overshoot past the formal edge of the convective boundary), which are varied in the Monte Carlo simulation. Typically, the mixing length is determined by calibrating a solar model to match the observed properties of the Sun, and this solar calibrated mixing length is used for calculating metal-poor stellar models. However, recent interferometric observations of the radius of the metal poor ([Fe/H] = −2.2) star HD 140283 by Creevey et al. (2015) require that stellar models for this star use a mixing length which is substantially below the solar value. Astroseismic studies using Kepler data have found a systematic metallicity dependance of the mixing length, with lower metallicity stars requiring the use of a lower mixing length (Bonaca et al. 2012; Tanner et al. 2014). To take this into account, the probability density distribution for the mixing length is taken to be a uniform distribution with $1.00 \leq \alpha \leq 1.70$, which is substantially below the solar calibrated mixing length ($\alpha \simeq 1.9$) for our stellar models.

The Monte Carlo simulation allows for the variation of both [α/Fe] and [Fe/H]. Table 6 provides mean [Fe/H] and [α/Fe] density distribution used in the MC simulations for each metal-poor subdwarf with the [Fe/H] standard deviation given from O'Malley et al. (submitted) as ±0.08 dex. Two different pairs of stars have very similar abundances, and a single MC simulation was run for a given pair of stars. In total, four different composition probability distributions were used, with 2000 MC isochrones being produced for each composition distribution and compared with the observations.

Table 6. Subdwarf Abundances

Subdwarf	[Fe/H]	[α/Fe] distributions
HIP 46120	−2.22	0.20 (50%), 0.40 (50%)
HIP 54639	−2.50	0.20 (80%), 0.40 (20%)
HIP 87788	−2.66	0.40 (25%), 0.60 (50%), 0.80 (25%)
HIP 103269	−1.83	0.20 (50%), 0.40 (50%)
HIP 106924	−2.23	0.20 (50%), 0.40 (50%)
HIP 108200	−1.83	0.20 (50%), 0.40 (50%)

The stellar evolution tracks cover a stellar mass range of 0.30 to 1.00 $M_\odot$ and provide the physical parameters for the simulated star from the zero age main-sequence through its evolution along the red giant branch. The stellar evolution tracks are used to produce isochrones in a standard fashion. The conversion from luminosities and effective temperatures to absolute magnitudes and colors used both synthetic color-temperature transformations from the PHOENIX model atmosphere grid (Hauschildt et al. 1999) and the semi-empirical color-temperature relations of VandenBerg & Clem (2003). The PHOENIX transformation isochrones will be referred to as ISO-P, and the VandenBerg & Clem (2003) transformed isochrones will be referred to as ISO-VC in the remainder of this paper.

The location of the stars in the color-absolute magnitude plane were compared to the isochrones for the stellar [Fe/H] using a reduced χ^2 minimization analysis. The χ^2 for each MC isochrone is defined as:

$$\chi^2 = \left(\frac{d}{\sigma}\right)^2 \tag{6}$$

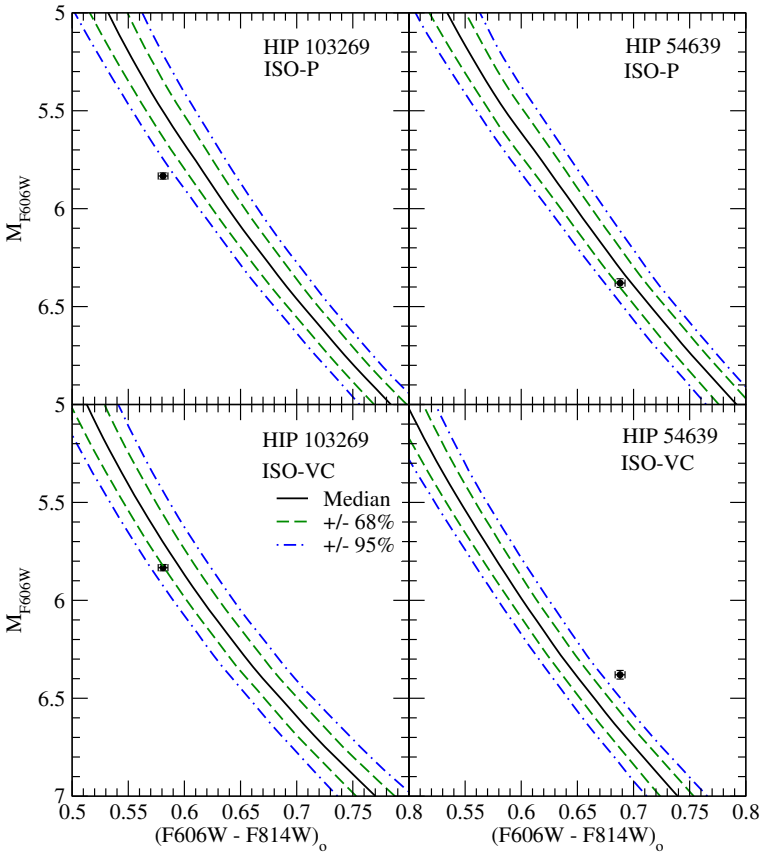

Figure 2. Comparison of HIP 103269 (left, with [Fe/H] = −1.83) and HIP 54639 (right, with [Fe/H] = −2.50) to Dartmouth stellar evolution isochrones. Shown here are the median isochrone (black solid), 1 σ (green dashed) and 2 σ (blue dot-dash) deviations for ISO-P (upper) and ISO-VC (lower). The color of HIP 103269 was over predicted by more than 95% of the ISO-P isochrones, while the color matches within 1 σ the ISO-VC isochrones. This is true for the four other main sequence stars, with the only exception being HIP 54639 whose color matches within 1 σ the ISO-P isochrones.

where d is the perpendicular distance between the target star and the main sequence (MS) of a 12 Gyr isochrone in a CMD and σ is the error associated with both the color and magnitude of our data. The reduced χ^2 for each model is

$$\chi^2_{red} = \frac{\sum_{n=1}^{5} \chi^2}{K} \tag{7}$$

where K is the number of degrees of freedom, which in this case is $K = 5$ as HIP 54639 was discarded from the fit (see below) and so leaving five stars to fit to our models with zero fit parameters.

A comparison of ISO-P versus ISO-VC fits to the field stars is shown for HIP 103269 in Figure 2. The color of each field star was overestimated by the median ISO-P isochrone while underestimated by the ISO-VC distribution. This was a general trend found for all the stars, except for HIP 54639. The ISO-VC [Fe/H] = −2.50 models showed strong disagreement in their comparisons to HIP 54639, with the models being too red, while the ISO-P models gave an acceptable fit to this stars. This is not too surprising, as HIP 54639 is much redder compared the other main sequence stars in our sample. HIP 54639 is also the faintest star in our sample, however there is no indication from deep globular cluster color-magnitude diagrams (Sarajedini et al. 2007) that the main sequence becomes markable redder at these magnitudes. As a result, it is most likely that the position of HIP 54639 is anomalous, perhaps due to it being an unresolved binary. As a result, HIP 54639 was removed from subsequent analysis for both color-temperature transformations.

The median deviation of the ISO-P models from the stars was 8.5 σ, with 99.8% falling outside of 2 σ and 98% falling outside 3 σ. For the ISO-VC models, the median deviation from the stars was 2.1σ ,with 56% of the isochrones falling outside of 2σ and only 21% outside of 3σ. The distribution of χ^2 values is shown in Figure 3 for two isochrones sets. It is clear from this analysis that the VandenBerg & Clem (2003) color-transformation does a much better job of matching the observed properties of metal-poor main sequence stars, and is the preferred color-transformation. These isochrones and their construction parameters will be used in determining the distances and ages of several GCs.

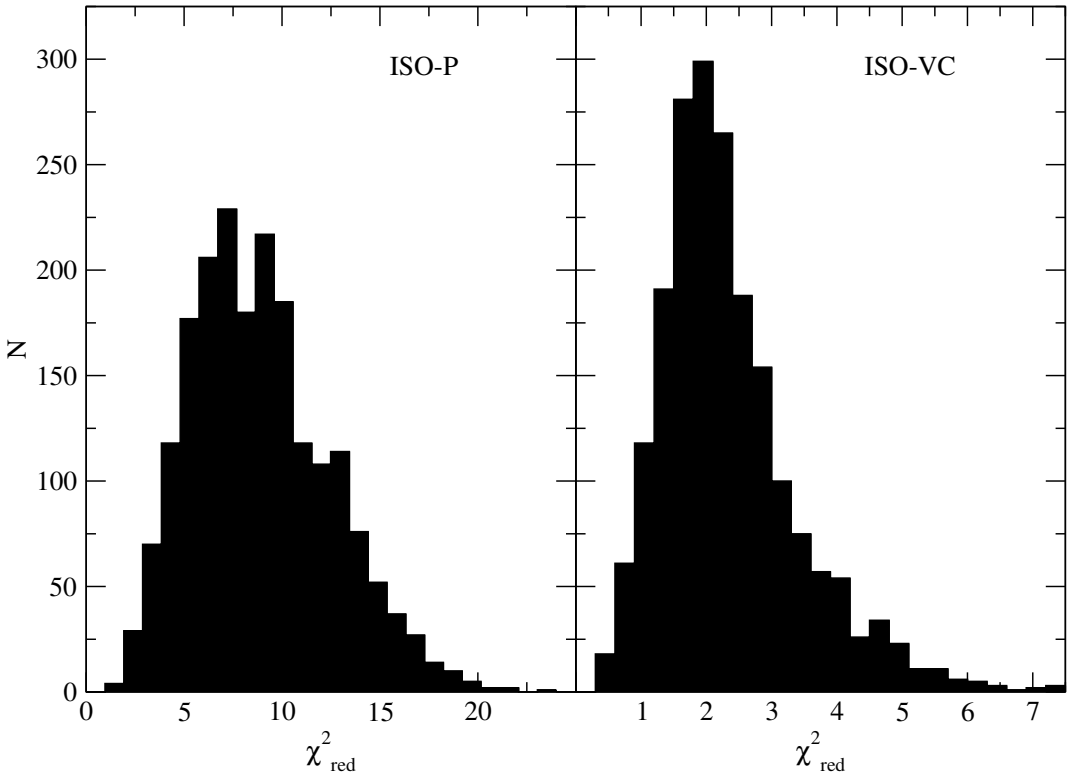

Figure 3. Distribution of χ^2 values shown for ISO-P (left) and ISO-V (right) using HST magnitudes.

4.1. *Stellar Parameters*

To understand the relationship between the input parameters and the goodness of fit to the parallax stars, it is instructive to perform an analysis of covariance (ANCOVA) on our results. An ANCOVA was conducted with the statistical software R (The R Core Team 2005) to test the effects and interactions of the input parameters on the fit of the models to the very metal-poor field stars. Table 7 provides the results of this analysis in the form of the minimal adequate model, both for the entire isochrone set, and just the ICO-VC isochornes. As was obvious in our initial investigation into the model fits (see Figure 3), the choice of color temperature relation produces very different distributions of fits for the same model parameters. The ANCOVA confirms this result, but also finds the underlying effects due to the input parameters themselves. Of the 20 input parameters used in constructing these models, six individual parameters produce highly significant effects on the resulting reduced χ^2 fit. As an example, the mixing length has a very strong effect on the model fit ($t = -30.5$). The effect is clearly evident when we look at the reduced χ^2 as a function of mixing length as shown in Figure 4, highlighting the advantages of the ANCOVA method of extracting this information from the complex dataset.

Table 7. ANCOVA of Model Input Parameters

Coefficients	Estimates	Std. Error	t-Value	Prob($<\|t\|$)
All Models				
Mixing length	−7.47	0.211	−35.46	$< 2 \times 10^{-16}$
$p + p \rightarrow {}^2\mathrm{H} + e^+ + \nu_e$	6.46	0.270	23.9	$< 2 \times 10^{-16}$
Diffusion Coefficients	2.41	0.293	8.25	$< 2 \times 10^{-16}$
Atmospheric $T(\tau)$	0.111	0.0196	5.69	1.4×10^{-8}
${}^3\mathrm{He} + {}^4\mathrm{He} \rightarrow {}^7\mathrm{Be} + \gamma$	11.90	2.29	5.21	2.0×10^{-7}
High-T opacities	2.73	1.02	2.67	0.0076
Only ISO-VC Models				

Table 7 continued on next page

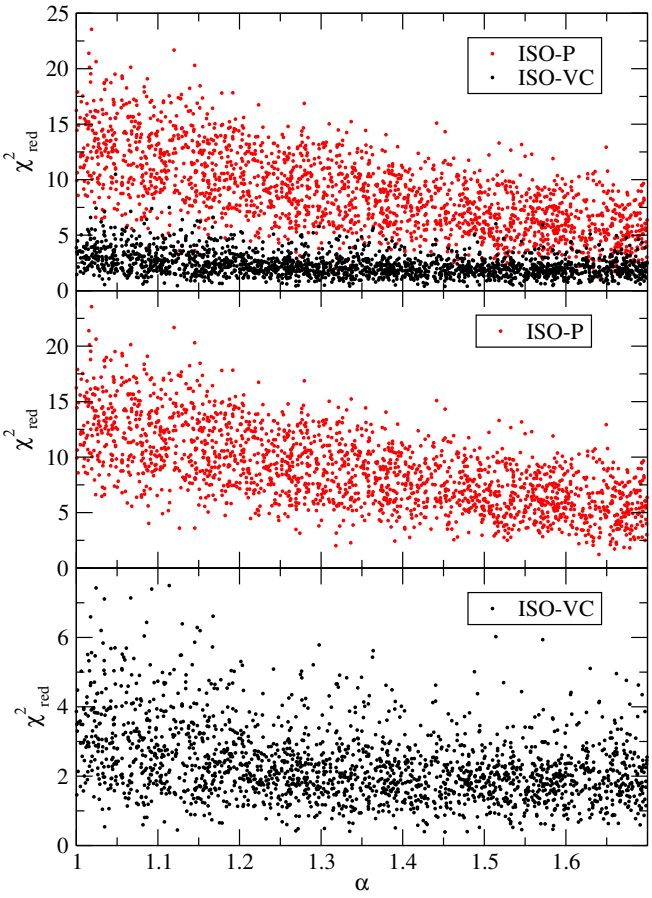

Figure 4. Reduced χ^2 as a function of mixing length, α. It is clear the color-temperature relation plays a large role in determining the goodness of fit and this effect must be accounted for in determining the best values for each parameter.

Table 7 *(continued)*

Coefficients	Estimates	Std. Error	t-Value	Prob($<\|t\|$)
Mixing Length	−1.37	0.097	−14.18	$< 2 \times 10^{-16}$
$p + p \rightarrow {}^2\mathrm{H} + e^+ + \nu_e$	1.18	0.124	9.47	$< 2 \times 10^{-16}$
[Fe/H]	1.10	0.245	4.50	7.1×10^{-6}
[α/Fe]	0.502	0.195	2.57	0.010
${}^3\mathrm{He} + {}^4\mathrm{He} \rightarrow {}^7\mathrm{Be} + \gamma$	−2.61	1.05	−2.48	0.013
High-T opacities	1.63	0.667	2.45	0.014

Regardless of which isochrone set we adopt, the most important physical parameters in determining the goodness of fit to the parallax stars are the mixing length and the $p + p$ reaction rate. These have been identified in previous studies as important uncertainties in lower mass, metal-poor stellar models (e.g. Chaboyer & Krauss 2002). The only surprise result is that we find the uncertainty in the ${}^3\mathrm{He} + {}^4\mathrm{He} \rightarrow {}^7\mathrm{Be} + \gamma$ reaction has an important impact on our fits to metal-poor stars. This is the slowest reaction in the PP-II chain, which becomes important at higher temperatures. The significance of this result is much lower with the ICO-VC models, and it would be worth investigating this issue in more detail with dedicated models.

5. DISTANCES AND AGES OF GCS

Main sequence fitting, whereby the absolute magnitude of stars with well determined parallexes are compared to the apparent magnitude of the main sequence in distance star clusters, is a commonly used technique to determine

the distances to star clusters. As mentioned in the introduction, a number of groups used *Hipparcos* parallaxes of metal-poor stars to determine the distances to globular clusters (e.g. Reid 1997; Gratton et al. 1997; Pont et al. 1998; Chaboyer et al. 1998; Carretta et al. 2000; Grundahl et al. 2002; Gratton et al. 2003). Since these works, it has become clear than many, if not all globular clusters contain multiple stellar populations (e.g. see reviews by Piotto 2009; Gratton et al. 2012). These different stellar populations are characterized by different chemical abundances, and it is likely that self-enrichment has occurred in many, if not all globular clusters. These multiple stellar populations have been identified using both spectroscopy (Gratton et al. 2012) and photometrically (Piotto 2009). It is unlikely that field stars experienced the same formation scenario, and the chemical composition of field stars is most similar to the primordial population of stars found in globular clusters. In order to use main sequence fitting to determine distances to GCs, it is important that one uses GC stars which have a primordial composition.

Photometric studies have found that when a blue filter is chosen (such as F225W or F336W) then the apparently tight principle sequences observed in ground based color-magnitude diagrams (CMDs) are often split into multiple sequences indicative of different stellar populations. For example, some globular clusters contain populations with enhanced helium abundances (e.g. Milone et al. 2012a; Milone 2015), and the different populations trace slightly different main sequences, with the helium enriched stars being redder on the main sequence than the stars with a primordial helium abundance. However, these distinct main sequences are often just seen when using blue filters, and when using the F606W and F814W filters, all the stars within the globular clusters NGC 6397 (Milone et al. 2012a) and NGC 6752 (Milone et al. 2013) fall along the same main sequence. This is not always the case, and in 47 Tuc (Milone et al. 2012b), NGC 2808 (Milone et al. 2015a) and NGC 7089 (Milone et al. 2015b) one sees a small offset on the main sequence between the helium enriched population and the primordial population when looking at the CMDs in the F606W and F814W filters.

The *HST* GC Treasury Project (Sarajedini et al. 2007), which obtained deep CMDs of a 65 globular clusters, was conducted in the F606W and F814W filters. The photometry from this project was downloaded from MAST, and used to determine the median ridge-line along the main sequence and subgiant branches for a number of GCs. In order to determine if this ridge-line traces the primordial stars, one needs to examine UV photometry to identify the different stellar populations. Piotto et al. (2015) have obtained UV photometry for most of GCs observed by Sarajedini et al. (2007). Careful analysis of this photometry has been used to identify multiple populations in most GCs studied (Milone et al. 2016). However, this photometry is not publicly available at this time, despite claims to the contrary in Piotto et al. (2015). Without having access to the UV photometry, which can be used to determine which stars are primordial, we need to adopt another approach to determine the location of the primordial main sequence in the F606W–F814W CMD.

UV CMDs are available for the clusters at Piotto's website, `http://groups.dfa.unipd.it/ESPG/treasury.php` in graphical form. In looking at these diagrams, clusters which show an offset between the primordial and helium enhanced stars on the main sequence in their F606W–F814W CMDs (47 Tuc, NGC 2808 and 7089), clearly show multiple main sequence populations in their UV CMDs, while for those clusters whose main sequence multiple populations are all on the same ridge-line in their F606W–F814W CMDs (NGC 6397 and 6752) one does not see evidence for multiple main sequence populations in the graphical UV CMDs. To ensure that the median ridge-lines in the F606W–F814W CMDs are tracing the primordial population, UV CMDs of a number of metal-poor GCs were examined, and those which showed no obvious evidence for multiple main sequence populations in their graphical UV CMDs were used in our main sequence fitting study. The location of the principle sequences (main sequence and turn-off region) in these clusters F606W–F814W CMDs is not affected by the presence of multiple populations, and the observed location of the principal sequences is indicative of the primordial population.

The location of the main sequence (in all filters) is sensitive to the abundance of iron and the $\alpha-$capture elements. To take this into account, distances will only be determined to GCs which have similar abundances to the HST parallax stars. The calibrating parallax stars have similar, although not identical, abundances to the primordial population of stars in our chosen GCs. To take into account the small differences in [Fe/H] and [α/Fe] between the HST parallax stars and the primordial GC stars, we do not directly compare the HST parallax stars to the main sequence stars in globular clusters. Instead, as described in the previous section, the HST parallax stars were used to determine what parameters yield theoretical isochrones which correctly predict the main sequence location of metal-poor stars. These same set of parameters, but with [Fe/H] and [α/Fe] values appropriate to a given GC are then used to generate isochrones and these isochrones are used to determine the distance and age of that GC.

5.1. *Sample Clusters*

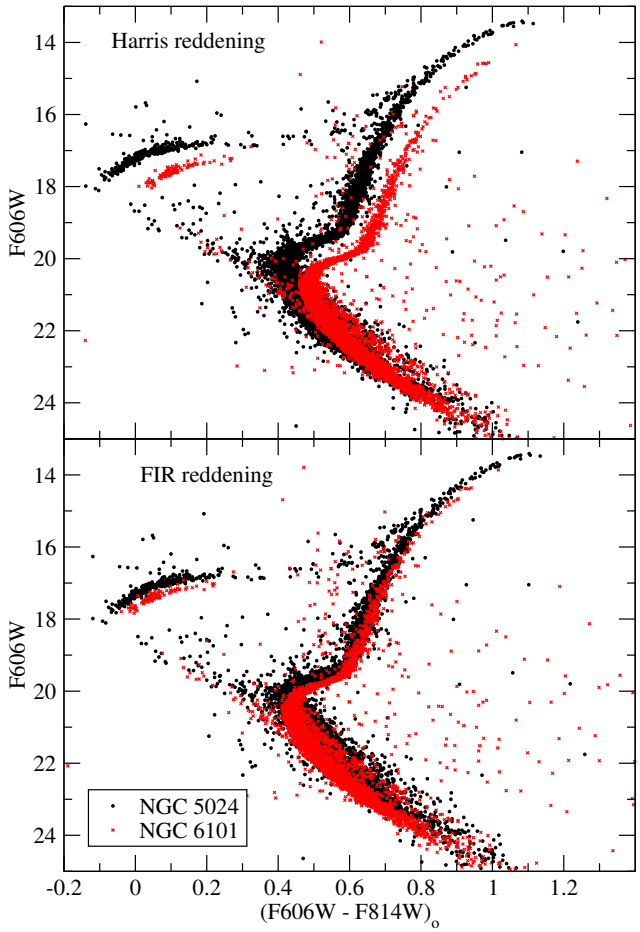

Figure 5. GCs of similar metallicity expected to have comparable RGB colors and HB magnitudes when adjusted to same relative distance. *Upper* - Dereddened CMDs of NGC 5024 (black) and NGC 6101 (red) using Harris (1996, version 2010) adjusted to same relative distance. We do not see overlapping RGBs nor HBs, suggesting reddening of one or both may be incorrect. *Bottom* - Dedreddened CMDs with Dutra et al. (2000) FIR reddening show much better agreement.

A sample of nine metal-poor ([Fe/H] < -1.9) and relatively un-reddened ($E(B-V) \leq 0.10$ mag) GCs with photometry from the *HST* GC Treasury Project (Sarajedini et al. 2007) were selected from the Harris (1996 version 2010) GC catalog for the main sequence fitting analysis. The photometry for these clusters was obtained with the same filters on ACS/WFC as our target metal-poor field stars. Hence, the photometry of both the GCs and our field stars are on the exact same system, which removes one possible source of systematic error from our analysis.

In studying the photometry of similar metallicity GCs, the Harris (1996; version 2010) reddening values give inconsistent colors of the RGB. This is demonstrated in Figure 5 where the red giant branch (RGB) color of NGC 5024 (black, [Fe/H] $= -2.10$ is compared to to NGC 6101 (red, [Fe/H] $= -1.98$). The top panel of Figure 5 uses the Harris (1996, version 2010) reddening and a relative distance modulus of 0.75 mag such that the MSs overlap. GCs of similar metallicity are expected to have comparable RGB colors and HB magnitudes when adjusted to the same relative distance; the fact that this is not seen suggests the reddening of one or both of these clusters may be incorrect. Due to this issue, the Dutra & Bica (2000) far-infrared (FIR) reddening values (based on the reddening maps of Schlegel et al. (1998) with reddening errors of ± 0.01 mag) were adopted for the MS fitting. The comparison of RGB colors for NGC 5024 and NGC 6101 using the FIR reddening values shows much better agreement in the bottom panel of Figure 5 using a relative distance modulus of 0.55 mag to match the MSs.

Some may question the use of FIR reddening for objects within the Milky Way due to the fact that FIR reddening values should represent the integrated dust column density throughout the whole Galaxy in any direction; therefore, FIR reddening values may over-estimate the reddening for nearby objects. However, the GCs used for this study are sufficiently far away and mostly out of the plane of the Galaxy that the reddening should not be over-estimated by the FIR reddening values. The FIR reddening values agree fairly well with the reddenings found by Dotter et al. (2010) and VandenBerg et al. (2013) who studied the cluster CMDs in detail to determine the cluster ages.

Table 8 provides information on the clusters' locations and reddening from Dutra & Bica (2000) along with metallicity from Harris (1996; version 2010) and the metallicity bin used in this study. The Sirianni et al. (2005) reddening relation for ACS/WFC of $E(F606W - F814W) = 0.984\,E(B-V)$ was used to convert the Dutra & Bica (2000) reddening to the HST photometric system.

Table 8. MS-fitting Cluster Data

Cluster	Messier	l(°)	b(°)	d_{Sun}(kpc)	$E(B-V)$	$E(B-V)_{FIR}$	Harris [Fe/H]	[Fe/H] bin
NGC 4590	M 68	299.63	36.05	10.2	0.05	0.06	-2.23	-2.25
NGC 5024	M 53	332.96	79.76	18.3	0.02	0.03	-2.10	-2.10
NGC 5053		335.69	78.94	16.4	0.04	0.02	-2.27	-2.25
NGC 5466		42.15	73.59	17.0	0.00	0.02	-2.31[a]	-2.36
NGC 6101		317.75	-15.82	15.3	0.05	0.10	-1.98	-1.96
NGC 6341	M 92	68.34	34.86	8.2	0.02	0.02	-2.34	-2.36
NGC 6809	M 55	8.80	-23.27	5.4	0.07	0.14	-1.94	-1.96
NGC 7078	M 15	65.01	-27.31	10.3	0.10	0.11	-2.37	-2.36
NGC 7099	M30	27.18	-46.83	8.0	0.03	0.05	-2.27	-2.25

[a] [Fe/H] of NGC 5466 taken from (Carretta et al. 2009).

5.2. *MS-Fitting Distances*

MS-fitting distances were determined for each cluster, taking into account observational uncertainty (including reddening errors). The best-fitting distance modulus was based on a fit of the median observed MS ridge-line shifted in both color and magnitude to the isochrone MS. For a given cluster, by visual inspection of the de-reddened CMD, the MS was defined in color and magnitude. The median MS ridge-line (within the color range of the field stars with parallaxes) was then calculated by determining the median color in 0.2 magnitude overlapping bins, therefore ensuring the median color found in each bin is not isolated. The median ridge-line was selected to ensure that the results are not affected by the red binary sequence found in GCs.

This median MS ridge-line is used to determine the distance modulus for each cluster using the 12 Gyr isochrones in our suite of models. The shape of the MS in the color range of field stars did not constrain the reddening. Shifting the median MS ridge-line in both color and magnitude led to equally well-fitting distance modulus for any color in the $E(F606W - F814W)$ range for that cluster. Therefore, we are able to calculate the distance modulus for the cluster based on the median $E(F606W - F814W)$ and propagate the uncertainty in the reddening to the uncertainty in the distance modulus using standard techniques. Since $A_v = 3.1\,E(B-V)$, the ± 0.01 uncertainty in reddening corresponds to a ± 0.03 uncertainty in the distance modulus for a given isochrone. The distance modulus determined with a given isochrone spans a range of ~ 0.7 mag, in the case of M92 the distance modulus ranges from 14.90 to 15.61 mag using ISO-P or from 14.60 to 15.21 mag using ISO-VC.

Not all isochrones have the same goodness of fit to the calibrating field stars with parallaxes, and the resultant distance modulus need to be weighted to take into account their probability of correctly representing actual stars. Specifically, a p-value is calculated for each isochrone based on its χ^2 vaule using $K = 5$ degrees of freedom. The weight applied to each isochrone was obtained by normalizing the p-value distribution. Table 9 gives the weighted mean distance modulus for each cluster. Since the ISO-P isochrones gave very poor fits to the calibrating field stars, they have very little weight when combined with the ISO-V isochrones, and the combined result, which represents our best estimate for the distance modulus to each cluster, is heavily weighted in favor of the ISO-VC isochrones. The average uncertainty in distance modulus is $\sigma_{DM} = 0.10$ mag which incorporates the photometric uncertainty and the uncertainty in stellar models. We see an offset of $\sim$0.15 mag between ISO-P and ISO-VC distance modulus determinations in the sense the ISO-P distance moduli are greater than the ISO-VC distance moduli. To illustrate the technique, Figure 6 compares data for M92 (NGC 6341) to the median ISO-VC isochrone and the calibrating field stars assuming the best fitting distance modulus shown in Table 9.

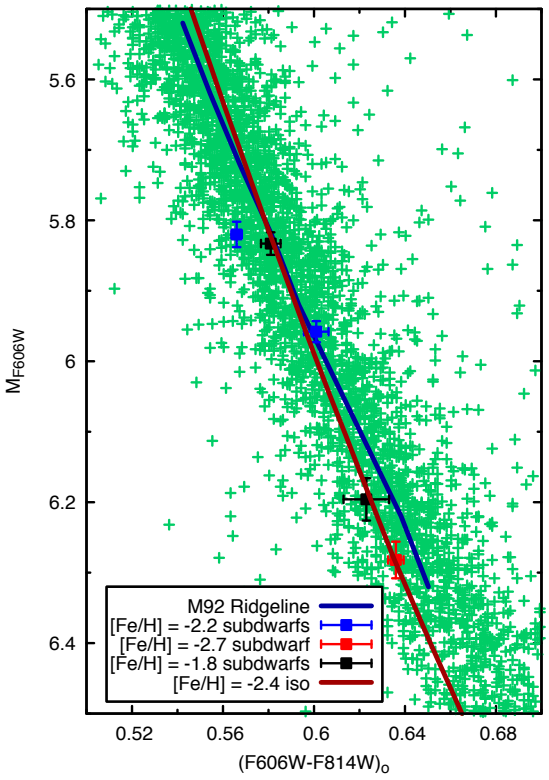

Figure 6. Comparison between the M92 data (green points, median ridgeline of the data blue solid line) from Sarajedini et al. (2007) with the calibrating field stars and the median ISO-VC isochrone from our Monte Carlo model with the M92 composition.

Table 9. Cluster Distance Modulus and Age Weighted by HST Fit

	ISO-P		ISO-V		Combined	
Cluster	$(m-M)_{F606W}$	Age (Gyr)	$(m-M)_{F606W}$	Age (Gyr)	$(m-M)_{F606W}$	Age (Gyr)
NGC 4590	15.63 ± 0.13	10.2 ± 1.2	15.52 ± 0.11	12.4 ± 1.2	15.52 ± 0.11	12.4 ± 1.2
NGC 5024	16.84 ± 0.13	10.3 ± 1.3	16.67 ± 0.10	13.2 ± 1.2	16.68 ± 0.10	13.2 ± 1.2
NGC 5053	16.58 ± 0.13	10.2 ± 1.2	16.47 ± 0.10	12.3 ± 1.2	16.47 ± 0.10	12.3 ± 1.2
NGC 5466	16.42 ± 0.13	11.0 ± 1.3	16.24 ± 0.10	13.9 ± 1.1	16.24 ± 0.10	13.9 ± 1.1
NGC 6101	16.35 ± 0.14	10.7 ± 1.5	16.21 ± 0.11	13.4 ± 1.4	16.21 ± 0.11	13.4 ± 1.4
NGC 6341	15.07 ± 0.13	10.3 ± 1.0	14.88 ± 0.10	13.2 ± 1.1	14.88 ± 0.10	13.2 ± 1.1
NGC 6809	14.50 ± 0.14	9.3 ± 1.5	14.35 ± 0.11	11.9 ± 1.4	14.35 ± 0.11	11.9 ± 1.4
NGC 7078	15.93 ± 0.12	9.2 ± 1.1	15.74 ± 0.10	12.1 ± 1.1	15.74 ± 0.10	12.1 ± 1.1
NGC 7099	15.12 ± 0.13	10.1 ± 1.2	15.02 ± 0.10	12.2 ± 1.2	15.02 ± 0.10	12.2 ± 1.2

5.3. *Cluster Ages*

The cluster distance modulus given by each individual isochrone is used to determine a distribution of ages for the cluster. The location of the sub-giant branch (SGB) in the clusters is compared to the SGB of the isochrone at ages ranging from 8 Gyr to 15 Gyr. The magnitude of the SGB is defined in Chaboyer et al. (1996) as the point brighter than the main-sequence turn-off (MSTO) and 0.05 mag redder. Chaboyer et al. (1996) showed the SGB provides the same level of theoretical uncertainty as the MSTO but is easier to measure on observational CMDs which leads to lower observational uncertainty. We visually inspect the CMDs of the clusters to determine the SGB and use a linear

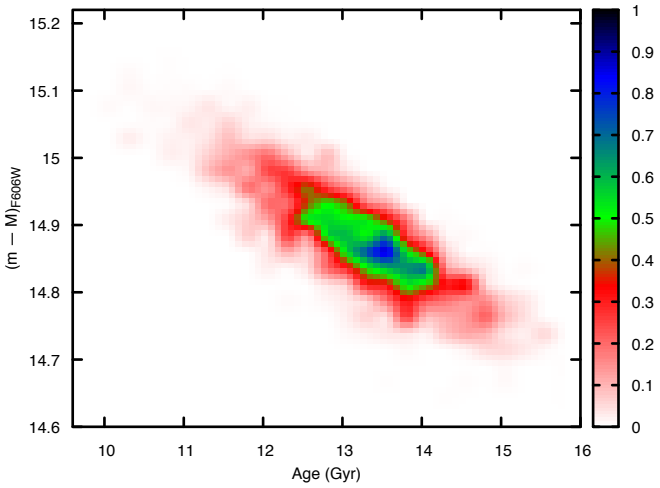

Figure 7. Probability distribution of the estimated age and distance modulus of M92 (on a relative scale) using ISO-VC isochrones. The inverse relationship between distance modulus and age is inherent in this analysis and is very clear.

regression of isochrone age vs. SGB magnitude to find the cluster age. The same weighting scheme is applied to this distribution of ages to derive our final ages based on the goodness of fit of each isochrone to the field star data. The ages for each GC are provided in Table 9, with average uncertainties of ~ 1.2 Gyr.

The offset of $\sim$0.15 mag in distance modulus between ISO-P and ISO-VC plays directly into the 2.6 Gyr offset we see in the ages between these two isochrone sets. Note that the inverse relationship between the distance modulus and age determined for each cluster is inherent in this analysis and is shown very clearly for M92 in Figure 7 which plots the ISO-VC age and distance muduli distributions (on a relative scale).

5.4. *Discussion*

Several sources provide estimates of GC distances and ages using varying methods of analysis. The Harris (1996; version 2010) GC catalog, which was used to determine initial estimates of [Fe/H] and $E(B-V)$ in this study, also provides distance moduli based on the horizontal branch (HB) magnitude observed in the CMD. On average, our best estimates for the distance moduli (from the combined models) are 0.30 mag larger than those listed in Harris (1996; version 2010). This difference is too large to be explained by simply the use of FIR reddening values. As shown earlier, a 0.01 mag increase in $E(B-V)$ corresponds to 0.03 mag increase in the distance modulus. The majority of our clusters used reddenings which are only 0.02 mag larger than listed by Harris (1996; version 2010), with a few exceptions increasing to 0.05 mag, suggesting that the difference in reddening estimates only accounts for ~ 0.08 mag of the difference in distance moduli.

Dotter et al. (2010) determine distance moduli by fitting isochrones to same *HST* photometry from Sarajedini et al. (2007) used in our study. We are using the same stellar evolution code as Dotter et al. (2010). On average, our distance moduli are 0.16 mag larger than those found by Dotter et al. (2010). The key difference[2] with the current study is that Dotter et al. (2010) did not have field star parallaxes to constrain their isochrones, and hence just used isochrones constructed with the best estimates for the various input parameters. This would correspond to our 'median' Monte Carlo isochrones and since the median isochrones do not provide the best fit to the parallax stars, the isochrones we are effectively using differ from those used by Dotter et al. (2010) even though we are using the same stellar evolution code.

Benedict et al. (2011) determined used HST FGS parallaxes for six RR Lyr stars and used RR Lyr stars as standard candles to determine distances to three GCs (NGC 4590, 6341 and 7078) in our sample. Using the same reddening values, the Benedict et al. (2011) distance moduli are, on average, smaller by 0.21 mag than the values determined in this paper. VandenBerg et al. (2013) (who adopted similar reddenings to those used in this study) fit theoretical zero-age horizontal branch models to determine the distance to six of the clusters in our sample and our distance

[2] In addition, Dotter et al. (2010) allowed both [Fe/H] and $E(B-V)$ to vary to find the best fit.

moduli are on average 0.24 mag larger than the VandenBerg et al. (2013) values.

Most recently, Watkins et al. (2015) have combined dynamical modeling with measurements of proper motion dispersions and line of slight velocity dispersions to determine dynamical distances to 15 GCs. To compare to our distance determinations, we converted the Watkins et al. (2015) distances to distance moduli using our preferred reddening value for each cluster. Only two of the cluster in our sample are in the Watkins et al. (2015) sample. For NGC 6341, Watkins et al. (2015) have $(m-M)_{F606W} = 14.81 \pm 0.07$ mag, which is similar to our distance moduli of $(m-M)_{F606W} = 14.88 \pm 0.10$ mag. In contrast, our distance modulus for NGC 7078 of $(m-M)_{F606W} = 15.74 \pm 0.10$ mag disagrees strongly with that found by Watkins et al. (2015) $(m-M)_{F606W} = 15.39 \pm 0.03$ mag.

In contrast to our distance results, our age determinations largely agree with previous work. For example, Dotter et al. (2010) determined the age of GCs by isochrone fitting from the TO through the SGB and their ages are 0.1 to 1.2 Gyr older than the combined ages in this work for seven out of the nine clusters. The ages derived for NGC 5466 and 6101 in this work are both older that that found in Dotter et al. (2010) by 0.9 and 0.4 Gyr, respectively. On average, our ages are 0.4 Gyr younger than those found by Dotter et al. (2010).

VandenBerg et al. (2013) also use the photometry provided in Sarajedini et al. (2007) to derive ages. In this case they allow for larger observational errorbars, but utilize the same Schlegel et al. (1998) reddening maps. The authors use the stellar evolution models from VandenBerg et al. (2012) and find the distance moduli using the zero-age horizontal branch magnitude. They determine ages by fitting isochrones from the TO through the SGB. The difference between the VandenBerg et al. (2012) ages and our ages span a range of 1.4 Gyr younger to 1.1 Gyr older, with a mean age difference of 0.2 Gyr.

We note that both Dotter et al. (2010) and VandenBerg et al. (2013) used a solar calibrated mixing length in their stellar models, while we use a mixing length which is well below the solar value in our isochrones. Changing the mixing length will impact the shape of the isochrones, and so it is likely that the ages derived by Dotter et al. (2010) and VandenBerg et al. (2013) would change if they adopted a non-solar mixing length. The luminosity of the SGB is only minimally affected by the choice of the mixing length (Chaboyer et al. 1996) and so the ages which we derive are less sensitive to the choice of the mixing length. The fact that our ages agree with previous work is fortuitous, as it appears that the younger ages one would expect from adopting the larger distance moduli find in this study, is offset by using a smaller mixing length, which increases our derived stellar ages.

6. SUMMARY

Accurate HST FGS1r parallaxes have been derived for 8 metal-poor stars. Six of these stars, with $-2.7 < [Fe/H] < -1.8$, are on the main sequence, and suitable for testing metal-poor stellar models and isochrones. These stars were also observed with ACS/WFC in the F606W and F814W filters, with uncertainties in their apparent magnitudes being less than 0.005 mag. Typical parallax uncertainties are of order 1%, leading to uncertainties of order ± 0.02 mag in the absolute magnitude of the stars. Using a Monte Carlo approach to take into account the uncertainties in the stellar models and isochrones, we found that isochrones constructed with the VandenBerg & Clem (2003) color calibration provide a much better fit to the location of the stars in a color-absolute magnitude diagram than those isochrones constructed using the the color calibration based upon the PHOENIX model atmospheres (Hauschildt et al. 1999).

Monte Carlo isochrones which provided an acceptable fit to the location of parallax stars were used to determine the distance (via main sequence fitting) and age (via the luminosity of the SGB) of nine metal-poor globular clusters (with $-2.4 < [Fe/H] < -1.9$) which have excellent ACS/WFC photometry from Sarajedini et al. (2007). Our distance moduli are of order 0.2 mag larger than previous distance determinations to metal-poor clusters. Thus, just as main sequence fitting results using *Hipparcos* parallaxes of more metal-rich stars than in our sample led to the conclusion that globular clusters were more distant than found by previous work (e.g. Reid 1997; Gratton et al. 1997; Pont et al. 1998; Chaboyer et al. 1998; Carretta et al. 2000; Grundahl et al. 2002; Gratton et al. 2003), we find that our *HST* parallaxes lead of metal-poor stars lead to main sequence fitting distances which are larger than previous work. The reason for this discrepancy is unclear, and warrants further study. In determining these main distances, we examined graphical UV CMDs in an attempt to only use GCs whose main sequences do not appear to show evidence for substantial helium enhancement (which would bias our results). Once the UV photometric data is publicly available, it would be useful to check that these results to ensure that location of the main sequence median ridge-line is reflective of the primordial stellar population.

Our absolute ages from these clusters range from 11.9 ± 1.4 Gyr to 13.9 ± 1.1 Gyr, in agreement with previous work. There is no convincing evidence that an intrinsic age difference exists between the different clusters. Averaging together the age of all nine clusters, leads to an absolute age of the oldest, most metal-poor globular clusters of 12.7 ± 1.0 Gyr, where the quoted uncertainty takes into account the known uncertainties in the stellar models and isochrones, along

with the uncertainty in the distance and reddening of the clusters.

Support for this work was provided by NASA through grants GO-11704 and GO-12320 from the Space Telescope Science Institute, which is operated by the Association of Universities for Research in Astronomy (AURA), Inc., under NASA contract NAS5-26555. This material is based upon work supported by the National Science Foundation Graduate Research Fellowship under Grant No. DGE-1313911. Any opinion, findings, and conclusions or recommendations expressed in this material are those of the authors(s) and do not necessarily reflect the views of the National Science Foundation. This publication makes use of data products from the Two Micron All Sky Survey, which is a joint project of the University of Massachusetts and the Infrared Processing and Analysis Center/California Institute of Technology, funded by NASA and the NSF. This research has made use of the SIMBAD database, operated at CDS, Strasbourg, France, and the NASA Astrophysics Data System Abstract Service. This work has made use of data from the European Space Agency (ESA) mission *Gaia* (http://www.cosmos.esa.int/gaia), processed by the *Gaia* Data Processing and Analysis Consortium (DPAC, http://www.cosmos.esa.int/web/gaia/dpac/consortium). Funding for the DPAC has been provided by national institutions, in particular the institutions participating in the *Gaia* Multilateral Agreement.

Facility: HST

Facility: McGraw-Hill

Facility: NMSU:1m

APPENDIX

A. FGS DATA REDUCTION

Astrometric data from the FGS are retrieved by download from the *HST* online archival retrieval system and then processed through the two-part FGS pipeline system. The low-level calibration pipeline extracts the astrometry measurements (usually from 1 to 2 minutes of fringe position information that was acquired at a 40 Hz rate, yielding several thousand discrete measurements) and after outlier removal (from cosmic ray hits etc.) calculates the median and performs a per-observation error estimation. The high-level calibration pipeline corrects the observations with the time-variant OFAD, compensates the velocity aberration, processes the time tags, and calculates the parallax factors with the JPL Earth orbit predictor (Standish 1990). The OFAD calibration is presented in several calibration papers (McArthur et al. 1997, 2002, 2006) and ongoing stability tests (LTSTABs) are used to maintain this calibration. FGS1R Instrumental systematics (such as intra-orbit drift and color and filter effects) are also corrected for. We have not found after 24 years of calibration additional systematics in our data at a level that is higher than our detection limit. Regression analysis between *Hipparcos* and *HST* parallax measurements has shown (with the exception of the Pleiades, Soderblom et al. (2005)) not only good agreement between the parallaxes determined by the two instruments, but also an *overestimation* of error in *HST* astrometric measurements (Benedict et al. 2007; McArthur et al. 2010).

The distribution of the reference stars in the field is shown in the Digital Sky Survey images in Figure A1. The position of each star is measured by the FGS sequentially. Each epoch contains multiple visits, of the metal-poor target and reference stars, providing $x(t)$ and $y(t)$ positions. These positions are measured in the *HST* reference frame in seconds of arc. During an orbit, positional drift occurs and was corrected for with an adaptable polynomial fitting routine amplified to model the high intra-orbit drift seen in some of these observations. The F583W filter was used for all observations. The observation dates, the number of measurements per epoch of the target metal-poor stars, the HST orientation angles and the number of plate parameters are listed on Table A1. Available only on-line as a machine-readable table (Table A2) is the *HST* astrometric data for the targets and their reference stars. The most current calibration the data should be retrieved from the *HST* online archival retrieval system and processed through the low and high level pipeline system.

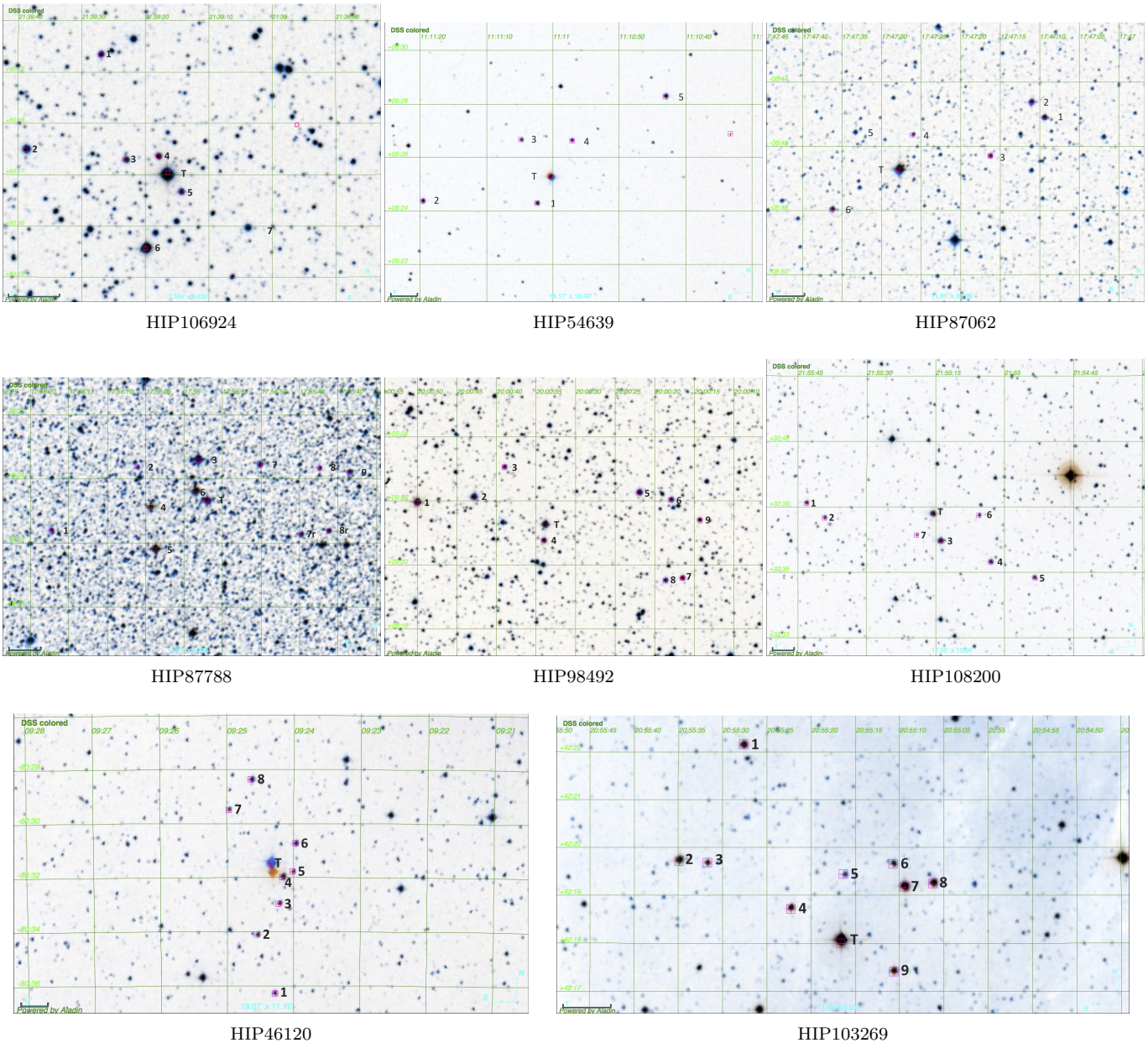

Figure A1. Metal-poor star fields with astrometric reference stars and target (T) labelled. The stars are listed in Table A8. The DSS images were made using *Aladin*.

Table A1. *HST*Astrometric Observation Targets Log

Orbit	Date	N_{obs}	*HST* Roll
HIP 46120			
1	27-Feb-2009	5	159.1263
2	5-Mar-2009	6	156.1014
3	15-Mar-2009	6	161.1411
4	7-Aug-2009	6	353.805
5	20-Aug-2009	6	353.805
6	28-Aug-2009	6	353.805
7	21-Aug-2010	6	353.8054
8	21-Feb-2011	5	168.5837
9	25-Feb-2011	6	169.1866
10	7-Aug-2011	6	353.8055
11	26-Aug-2011	6	353.8055
HIP 54639			
1	9-Dec-2008	7	256.9946
2	15-Dec-2008	5	256.9946
3[a]	21-Dec-2008	7	256.9946
4	23-Mar-2010	7	67.50748
5	3-Jun-2010	7	67.50748
6	17-Jun-2010	7	67.50748
7	9-Dec-2010	7	256.9946
8	4-Jun-2011	7	67.78232
9	17-Jun-2011	7	67.78232
10	9-Dec-2011	7	256.9946
11	14-Dec-2011	7	256.9946
HIP 87062			
1	9-Mar-2009	5	270.9999
2	13-Mar-2009	5	270.9999
3	10-May-2009	5	271.9994
4	24-Jul-2009	5	88.99068
5	11-Sep-2009	5	88.99068
6	18-Sep-2009	5	88.99068
7	19-Sep-2010	5	88.99069
8	3-Mar-2011	5	263.3456
9	18-Mar-2011	5	271.5355
10	2-Sep-2011	5	88.9907
11	16-Sep-2011	5	88.9907
HIP 87788			
1	20-Mar-2009	4	270.0006
2	2-Apr-2009	6	270.0006
3	18-Jul-2009	6	84.99417

Table A1 continued on next page

Table A1 *(continued)*

Orbit	Date	N_{obs}	*HST* Roll
4	11-Sep-2009	6	84.99417
5[b]	22-Sep-2009	6	84.99417
6	12-Oct-2009	6	87.49677
7	1-Jun-2010	6	270.0006
8	22-Sep-2010	6	84.99417
9	20-Mar-2011	4	270.0006
10	30-Mar-2011	6	270.0006
11	10-Sep-2011	6	84.99417
12	22-Sep-2011	6	84.99417
	HIP 98492		
1	25-Apr-2009	5	287.0096
2	4-May-2009	6	287.0096
3	19-Sep-2009	6	99.99505
4	16-Oct-2009	6	99.99505
5	26-Oct-2009	6	99.99505
6	1-Jun-2010	6	289.0107
7	24-Oct-2010	6	99.99506
8	24-Apr-2011	5	287.0096
9	13-May-2011	6	287.0096
10	22-Sep-2011	6	99.99506
11	26-Oct-2011	6	99.99506
	HIP 103269		
1	16-Jun-2009	7	302.1005
2	15-Nov-2009	7	116.8969
3	25-Nov-2009	7	116.8969
4	30-Nov-2009	7	116.8969
5	26-May-2010	7	302.1005
6	6-Jun-2010	7	302.1005
7	31-Oct-2010	7	116.8969
8	26-May-2011	7	302.1005
9	16-Jun-2011	7	302.1005
10	15-Nov-2011	7	116.8969
11	30-Nov-2011	7	116.8969
	HIP 106924		
1	19-Dec-2008	5	142.711
2	2-Jan-2009	5	142.711
3[a]	5-Jan-2009	6	142.711
4	2-Jul-2009	6	323.2631
5	12-Jul-2009	6	323.2631
6	20-Jul-2009	6	323.2631
7	2-Aug-2010	6	336.3016
8	19-Dec-2010	5	142.7101
9	7-Jan-2011	6	142.7101

Table A1 continued on next page

Table A1 *(continued)*

Orbit	Date	N_{obs}	*HST* Roll
10	4-Jul-2011	6	323.2635
11	21-Jul-2011	6	323.2635
	HIP 108200		
1	19-Jun-2009	6	290.0325
2	13-Nov-2009	5	109.956
3	18-Nov-2009	6	109.956
4	4-Dec-2009	6	109.956
5	21-May-2010	6	290.0323
6	31-May-2010	6	290.0323
7	3-Dec-2010	5	109.9559
8	21-May-2011	6	290.0322
9	18-Jun-2011	6	290.0322
10	11-Nov-2011	6	109.9557
11	4-Dec-2011	6	109.9557

[a] FGS1R AMA-Adjustment after this observation

[b] Observation set failed

Table A2. Table Format for Astrometric Data for Target and Reference Stars [a]

Column	Format	Desription
1	A9	HST Observation ID
2	A8	HST observing mode; POSITION or TRANSFER
3	A10	Raw target ID from proposal
4	I5	Proposal number of observations
5	I4	tar number of observation from proposal
6	F5.2	Predicted V band magnitude
7	F5.2	Actual V band magnitude
8	F8.5	Predicted Right Ascension; decimal degrees (J2000)
9	F8.5	Predicted Declination; decimal degrees (J2000)
10	F8.5	Right Ascension of V1 telescope axis; degrees (1)
11	F8.5	Declination of V1 telescope axis; degrees (1)
12	F8.4	Roll about V3 of telescope
13	F12.6	X position of telescope
14	F12.6	Y position of telescope
15	F12.6	Z position of telescope
16	F9.6	X velocity of telescope
17	F9.6	Y velocity of telescope
18	F9.6	Z velocity of telescope
19	F16.8	Observation Julian Date; corrected

Table A2 continued on next page

Table A2 *(continued)*

Column	Format	Desription
20	F14.8	Modified Julian observation time
21	I4	Year of observation
22	I3	Day of observation
23	A8	The hour:min:sec of observation
24	I1	FGS used as the astrometer
25	A5	Filter used for observation
26	I3	Set number of observation group
27	F13.9	Earth plus HST X velocity
28	F13.9	Earth plus HST Y velocity
29	F13.9	Earth plus HST Z velocity
30	F10.5	Uncorrected X position calculated by average
31	F9.5	Uncorrected Y position calculated by average
32	F7.5	Standard deviation in Xave
33	F7.5	Standard deviation in Yave
34	F8.5	XY correlation
35	F13.10	XY covariance
36	F14.9	Uncorrected X position calculated by median
37	F11.7	Uncorrected Y position calculated by median
38	F7.5	X median average deviation
39	F7.5	Y median average deviation
40	F6.2	Seconds of FINELOCK data
41	I4	Number of samples from FINELOCK interval
42	A5	Instrument velocity aberration measured from
43	I1	S FGS velocity aberration measured from
44	F13.9	X position of velocity aberration
45	F11.7	Y position of velocity aberration
46	I1	Dominant FGS guider
47	F10.4	Sum of pmts
48	F9.4	pmt from channel xa
49	F9.4	pmt from channel xb
50	F9.4	pmt from channel ya
51	F9.4	pmt from channel yb
52	I3	Number of samples for background
53	I4	Number of samples for walkdown pmt diff/sum in X axis
54	F7.4	X pmt diff/sum from fine lock dv interval
55	F7.4	X pmt diff/sum from walkdown interval
56	F6.4	Reference X axis S_curve inverse slope of Upgren69
57	F9.6	X centroid shift in arcseconds; add to Xmed
58	I4	Number of samples for walkdown pmt diff/sum in Y axis
59	F7.4	Y pmt diff/sum from fine lock dv interval
60	F7.4	Y pmt diff/sum from walkdown interval
61	F6.4	Reference Y axis S_curve inverse slope of Upgren69
62	F9.6	Y centroid shift in arcseconds; add to Ymed

Table A2 continued on next page

Table A2 *(continued)*

Column	Format	Desription
63	F8.3	Course track X position
64	F7.3	Course track Y position
65	I6	Star selector position; theta A
66	I6	Star selector position; theta B
67	E11.5	Variance of X
68	E11.5	Variance of Y
69	E11.5	Median average deviation variance of X
70	E11.5	Median average deviation variance of Y
71	F11.4	Predicted star selector position; theta A
72	F11.4	Predicted star selector position; theta B
73	F11.9	Interpolated rhoA lever arm
74	F11.9	Interpolated kA lever arm
75	F11.9	Spacecraft quaternion
76	F12.9	Spacecraft quaternion
77	F12.9	Spacecraft quaternion
78	F12.9	Spacecraft quaternion
79	F12.9	Parallax factor alpha
80	F12.9	Parallax factor delta
81	E14.7	Sinfit position correction for X
82	F14.9	Final X corrected position with polynomial drift correction
83	F13.9	Final Y corrected position with polynomial drift correction
84	A9	Target name

[a] Table A2 is published in its entirety in the electronic edition. The column descriptions and format are shown here for guidance regarding its form and content.

A.1. *Reference Star Spectroscopy and Photometry*

We obtained spectra of the reference frame stars for the northern targets using the Dual Imaging Spectrograph[2] ("DIS") on the 3.5 m telescope at the Apache Point Observatory. DIS simultaneously obtains spectra covering blue and red spectral regions, providing dispersions of 0.62 Å/pix in the blue, and 0.58 Å/pix in the red with the high resolution gratings (1,200 line/mm). For HIP46120 and HIP54639, we obtained spectra of the reference frame stars using the R−C Spectrograph[3] on the Blanco 4 m telescope at Cerro Tololo Interamerican Observatory (program 2009A-0009). The KPGL1 grating was used, and with the "Loral 3K" detector, provided a dispersion of 1.01 Å/pix.

Optical photometry for the fields all of the program stars, except HIP46120, was procured using the robotic New Mexico State University (NMSU) 1 m telescope (Holtzman 2010) at Apache Point Observatory and the MDM 1.3 m telescope. The NMSU 1 m is equipped with an E2V 2048 sq. CCD camera, and the standard Bessell $UBVRI$ filter set. THE MDM 1.3 m data was obtained with a STA-0500 4062 sq. CCD camera and a standard BVRI filter set. Photometry of the field of HIP46120 was obtained using the Tek2K CCD imager[4] on the SMARTS 0.9 m telescope at CTIO (program 2009A-0009). The images of the program object fields, along with the appropriate calibration data, were obtained in the usual fashion, reduced using IRAF, and flux calibrated with observations of Landolt standards.

We use the transformations provided in Carpenter (2001) to convert the 2MASS JHK values to the Bessell & Brett (1988) system. Table A3 lists $VJHK$ photometry for the target and reference stars indicated in Figures A1. Figure A2

[2] http://www.apo.nmsu.edu/arc35m/Instruments/DIS/

[3] http://www.ctio.noao.edu/spectrographs/4m_R-C/4m_R-C.html

[4] http://www.ctio.noao.edu/noao/content/tek2k

show the $(J-K)$ vs. $(V-K)$ color-color diagrams with reference stars and targets labeled.

Table A3. V and Near-IR Photometry of Target and Reference Stars

ID	V	$U-B$	$B-V$	$V-R$	$V-I$	J	H	K
			HIP 46120					
Ref-1	14.34 ± 0.02	0.13 ± 0.04	0.74 ± 0.04	0.42 ± 0.03	0.84 ± 0.03	12.91	12.52	12.49
Ref-2	13.96 ± 0.02	0.22 ± 0.04	0.81 ± 0.04	0.44 ± 0.03	0.9 ± 0.03	12.44	12.05	11.99
Ref-3	14.02 ± 0.02	0.59 ± 0.04	1.00 ± 0.04	0.53 ± 0.03	1.05 ± 0.03	12.23	11.73	11.65
Ref-4	12.58 ± 0.02	0.23 ± 0.04	0.75 ± 0.04	0.39 ± 0.03	0.82 ± 0.03	11.19	10.88	10.81
Ref-5	14.76 ± 0.02	0.35 ± 0.05	0.82 ± 0.04	0.43 ± 0.03	0.86 ± 0.03	13.3	12.97	12.85
Ref-6	13.48 ± 0.02	0.48 ± 0.04	0.89 ± 0.04	0.47 ± 0.03	0.96 ± 0.03	11.82	11.45	11.33
Ref-7	14.91 ± 0.02	0.81 ± 0.06	1.01 ± 0.05	0.6 ± 0.03	1.13 ± 0.03	12.99	12.48	12.39
Ref-8	13.21 ± 0.02	0.59 ± 0.04	1.03 ± 0.04	0.56 ± 0.03	1.1 ± 0.03	11.32	10.8	10.72
HIP 46120[a]								
			HIP 54639					
Ref-1	13.87 ± 0.02	0 ± 0.1	0.47 ± 0.04	0.28 ± 0.03	0.59 ± 0.03	12.89	12.57	12.52
Ref-2	13.45 ± 0.02	0.9 ± 0.13	0.97 ± 0.07	0.53 ± 0.03	1.01 ± 0.03	11.71	11.2	11.07
Ref-3	14.72 ± 0.02	1.05 ± 0.2	1.09 ± 0.1	0.56 ± 0.03	1.07 ± 0.03	12.81	12.18	12.03
Ref-4	14.72 ± 0.02	1.28 ± 0.2	1.06 ± 0.1	0.66 ± 0.03	1.24 ± 0.03	12.66	11.99	11.91
Ref-5	13.23 ± 0.02	1.41 ± 0.14	1.24 ± 0.05	0.78 ± 0.03	1.46 ± 0.03	10.81	10.17	10.05
HIP 54639								
			HIP 87062					
Ref-1	13.36 ± 0.02	0.51 ± 0.1	1.07 ± 0.04	0.67 ± 0.03	1.36 ± 0.03	10.99	10.58	10.25
Ref-2	13.32 ± 0.02	2.06 ± 0.1	1.88 ± 0.04	1.13 ± 0.03	2.13 ± 0.03	9.55	8.66	8.32
Ref-3	14.58 ± 0.02	0.77 ± 0.1	1.24 ± 0.05	0.73 ± 0.03	1.44 ± 0.03	12.05	11.55	11.42
Ref-4	15.67 ± 0.04	0.77 ± 0.1	1.27 ± 0.09	0.81 ± 0.04	1.63 ± 0.03	12.82	12.34	12.12
Ref-5	14.65 ± 0.02	2.02 ± 0.1	2.02 ± 0.07	1.27 ± 0.03	2.47 ± 0.03	10.32	9.36	9.05
Ref-6	13.77 ± 0.02	0.67 ± 0.1	1.05 ± 0.04	0.62 ± 0.03	1.31 ± 0.03	11.5	11.16	11.04
HIP 87062	10.57 ± 0.02	-0.06 ± 0.1	0.59 ± 0.04	0.37 ± 0.03	0.83 ± 0.03	9.17	8.86	8.77
			HIP 87788					
Ref-1	14.45 ± 0.02	1.32 ± 0.22	2.35 ± 0.05	1.54 ± 0.03	2.97 ± 0.03	9.24	7.96	7.35
Ref-2	14.57 ± 0.02	1.64 ± 0.24	2.13 ± 0.05	1.23 ± 0.03	2.34 ± 0.03	10.38	9.36	9.16
Ref-3	10.55 ± 0.02	1.85 ± 0.1	1.63 ± 0.04	0.96 ± 0.03	1.81 ± 0.03	7.33	6.47	6.22
Ref-4	11.98 ± 0.02	-0.06 ± 0.1	0.38 ± 0.04	0.18 ± 0.03	0.44 ± 0.03	11.12	11.02	10.96
Ref-5	11.04 ± 0.02	0.21 ± 0.1	0.54 ± 0.04	0.26 ± 0.03	0.62 ± 0.03	9.87	9.73	9.63
Ref-6	11.55 ± 0.02	1.36 ± 0.1	1.39 ± 0.04	0.75 ± 0.03	1.47 ± 0.03	8.91	8.24	8.06
Ref-7	13.49 ± 0.02	1.82 ± 0.15	2.06 ± 0.04	1.39 ± 0.03	2.93 ± 0.03	8.47	7.42	7.04
Ref-8	13.75 ± 0.02	1.96 ± 0.15	1.85 ± 0.04	1.04 ± 0.03	1.97 ± 0.03	10.18	9.39	9.01
Ref-9	13.47 ± 0.02	1.05 ± 0.13	1.3 ± 0.04	0.71 ± 0.03	1.42 ± 0.03	10.85	10.25	10.05
Ref-7R	14.41 ± 0.02	±	2.16 ± 0.04	±	±			8.61
Ref-8R	13.52 ± 0.02	±	0.88 ± 0.04	±	±			11.33
HIP 87788	11.33 ± 0.02	-0.16 ± 0.07	0.74 ± 0.04	0.39 ± 0.03	0.87 ± 0.03	9.94	9.54	9.46
			HIP 98492					
Ref-1	11.18 ± 0.02	-0.06 ± 0.06	0.08 ± 0.03	0.03 ± 0.02	0.12 ± 0.02	10.93	10.96	10.94

Table A3 continued on next page

Table A3 *(continued)*

ID	V	$U-B$	$B-V$	$V-R$	$V-I$	J	H	K
Ref-2	11.89 ± 0.02	1.53 ± 0.06	1.31 ± 0.03	0.7 ± 0.02	1.3 ± 0.02	9.58	8.97	8.79
Ref-3	14.19 ± 0.02	0.75 ± 0.1	1.01 ± 0.03	0.56 ± 0.02	1.07 ± 0.02	12.26	11.97	11.69
Ref-4	13.24 ± 0.02	0.28 ± 0.06	0.74 ± 0.03	0.4 ± 0.02	0.79 ± 0.02	11.84	11.55	11.45
Ref-5	12.35 ± 0.02	0.99 ± 0.06	1.04 ± 0.03	0.55 ± 0.02	1.05 ± 0.02	10.48	10.02	9.91
Ref-6	13.32 ± 0.02	2.01 ± 0.1	1.64 ± 0.04	1.02 ± 0.02	2.13 ± 0.02	9.74	8.87	8.61
Ref-7	13.61 ± 0.02	0.12 ± 0.06	0.57 ± 0.03	0.32 ± 0.02	0.66 ± 0.02	12.5	12.27	12.2
Ref-8	13.71 ± 0.02	1.7 ± 0.1	1.44 ± 0.03	0.82 ± 0.02	1.56 ± 0.02	10.98	10.22	10.06
Ref-9	14 ± 0.02	0.28 ± 0.08	0.7 ± 0.03	0.38 ± 0.02	0.77 ± 0.02	12.64	12.4	12.31
HIP 98492	11.58 ± 0.02	-0.03 ± 0.06	0.65 ± 0.03	0.39 ± 0.02	0.8 ± 0.02	10.15	9.8	9.72
HIP 103269								
Ref-1	13.04 ± 0.02	0.85 ± 0.1	0.99 ± 0.04	0.59 ± 0.03	1.13 ± 0.03	11.13	10.61	10.54
Ref-2	12.37 ± 0.02	0.1 ± 0.1	0.65 ± 0.04	0.39 ± 0.03	0.78 ± 0.03	11.11	10.79	10.75
Ref-3	14.64 ± 0.02	0.34 ± 0.11	0.8 ± 0.04	0.46 ± 0.03	0.93 ± 0.03	13.09	12.7	12.7
Ref-4	13.36 ± 0.02	0.18 ± 0.1	0.67 ± 0.04	0.37 ± 0.03	0.77 ± 0.03	12.11	11.83	11.78
Ref-5	15.46 ± 0.02	-.- ± 2.61	0.07 ± 1.85	0.03 ± 3.58	0.03 ± 9.42	8.13	7.69	
Ref-6	14.14 ± 0.02	0.47 ± 0.11	0.82 ± 0.04	0.46 ± 0.03	0.93 ± 0.03	12.68	12.31	12.29
Ref-7	11.59 ± 0.02	0.03 ± 0.1	0.55 ± 0.04	0.3 ± 0.03	0.65 ± 0.03	10.56	10.29	10.26
Ref-8	12.77 ± 0.02	0.24 ± 0.1	0.72 ± 0.04	0.35 ± 0.03	0.8 ± 0.03	11.43	11.11	11.05
Ref-9	13.49 ± 0.02	0.26 ± 0.1	0.77 ± 0.04	0.39 ± 0.03	0.83 ± 0.03	12.13	11.73	11.71
HIP 103269	10.28 ± 0.02	-0.45 ± 0.1	0.64 ± 0.04	0.38 ± 0.03	0.79 ± 0.03	9.03	8.7	8.61
HIP 106924								
Ref-1	14.64 ± 0.02	0.5 ± 0.1	1.06 ± 0.04	0.7 ± 0.03	1.28 ± 0.03	12.47	12.05	11.89
Ref-2	13.25 ± 0.02	1.71 ± 0.1	1.64 ± 0.04	0.97 ± 0.03	1.86 ± 0.03	10.09	9.28	9.07
Ref-3	14.73 ± 0.02	1.5 ± 0.11	1.54 ± 0.05	0.92 ± 0.03	1.76 ± 0.03	11.66	11	10.78
Ref-4	14.3 ± 0.02	0.35 ± 0.1	0.76 ± 0.04	0.47 ± 0.03	0.97 ± 0.03	12.65	12.48	12.33
Ref-5	14.63 ± 0.02	1.68 ± 0.12	1.61 ± 0.04	0.93 ± 0.03	1.75 ± 0.03	11.64	10.89	10.68
Ref-6	11.44 ± 0.02	-0.02 ± 0.1	0.56 ± 0.04	0.28 ± 0.03	0.62 ± 0.03	10.41	10.17	10.14
Ref-7	14.1 ± 0.02	1.74 ± 0.11	1.8 ± 0.04	1.05 ± 0.03	2.02 ± 0.03	10.59	9.71	9.47
HIP 106924	10.42 ± 0.02	-0.36 ± 0.1	0.57 ± 0.04	0.43 ± 0.03	0.87 ± 0.03	9.04	8.86	8.57
HIP 108200								
Ref-1	13.06 ± 0.02	0.25 ± 0.1	0.69 ± 0.04	0.37 ± 0.03	0.76 ± 0.03	11.78	11.51	11.4
Ref-2	13.65 ± 0.02	1.17 ± 0.1	1.15 ± 0.04	0.6 ± 0.03	1.18 ± 0.03	11.57	10.97	10.88
Ref-3	11.15 ± 0.02	1.32 ± 0.1	1.17 ± 0.04	0.65 ± 0.03	1.22 ± 0.03	9.06	8.49	8.34
Ref-4	12.18 ± 0.02	1.41 ± 0.1	1.3 ± 0.04	0.71 ± 0.03	1.36 ± 0.03	9.79	9.07	8.95
Ref-5	13.18 ± 0.02	0.16 ± 0.1	0.65 ± 0.04	0.35 ± 0.03	0.72 ± 0.03	11.96	11.65	11.6
Ref-6	13.89 ± 0.02	1.42 ± 0.1	1.25 ± 0.04	0.66 ± 0.03	1.24 ± 0.03	11.7	11.07	10.93
Ref-7	15.29 ± 0.02	0.16 ± 0.1	0.67 ± 0.04	0.41 ± 0.03	0.84 ± 0.03	13.88	13.61	13.43
HIP 108200	10.97 ± 0.02	-0.09 ± 0.1	0.67 ± 0.04	0.4 ± 0.03	0.83 ± 0.03	9.58	9.21	9.1

[a] Target saturated on all images

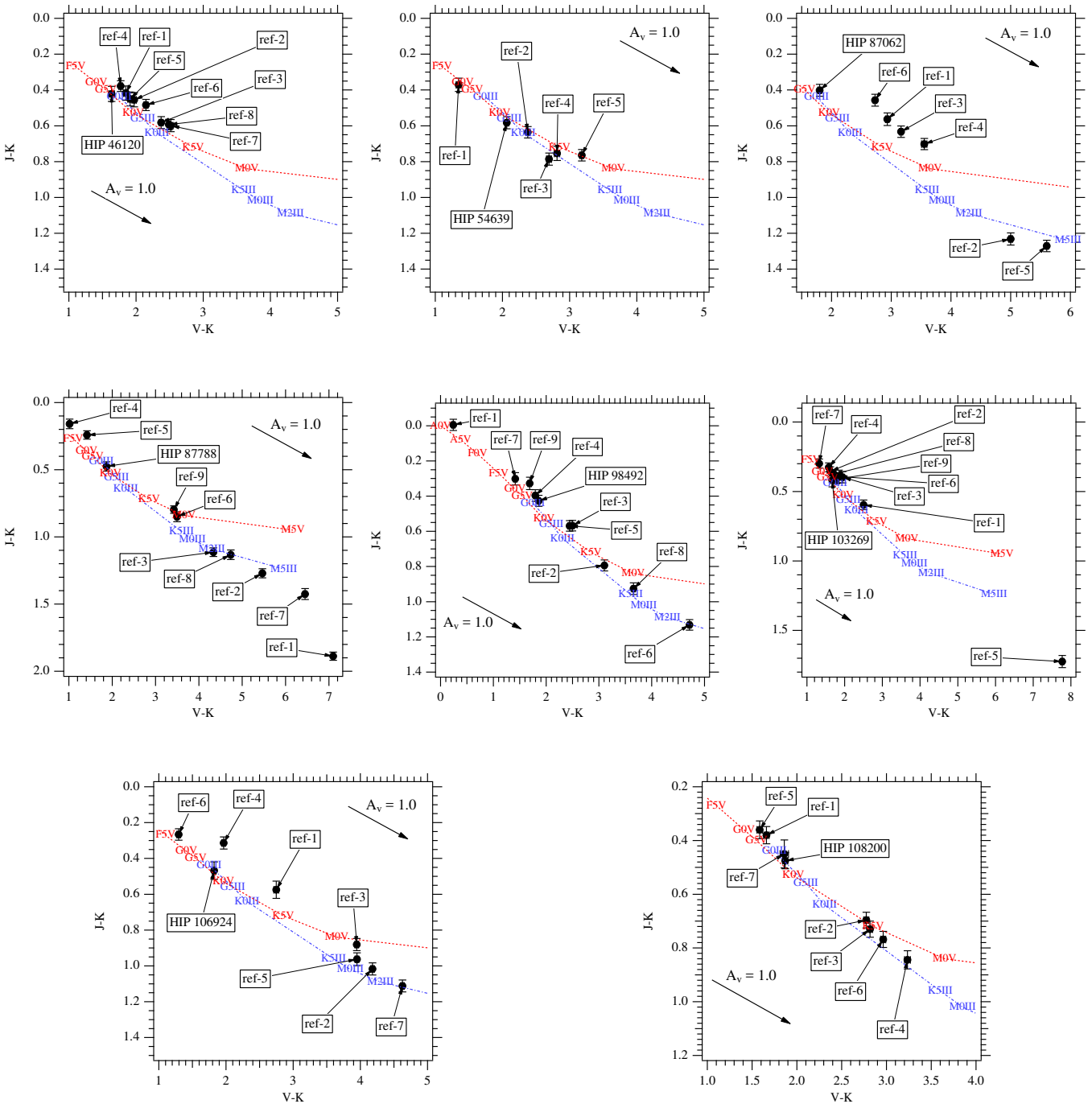

Figure A2. $(J-K)$ vs. $(V-K)$ color-color diagram for stars in the *HST* field identified in Table A3. The dashed line is the locus of dwarf (luminosity class V) stars of various spectral types; the dot-dashed line is for giants (luminosity class III).

A.2. *Spectroscopy, Luminosity Class and Reduced Proper Motion*

The derived absolute magnitudes are crucially dependent on the assumed stellar luminosities, a parameter impossible to obtain for all but the latest type stars using only Figure A2. To aid in the spectral classification of the reference stars we have compiled an extensive set of template spectra covering a large range of temperature and luminosity classes in support of our various FGS programs on both the APO 3.5 m, and the Blanco 4 m. We perform MK classification of each of the reference frame stars with respect to these templates, as well as use the temperature and luminosity classification characteristics listed in Yamashita et al. (1978). For the DIS spectra, our temperature classifications

are generally good to ± 1 subclass. For the lower resolution CTIO data, however, there is more uncertainty, and we generally obtain spectral classifications with uncertainties of ± 2 subclasses.

To confirm the luminosity classes we obtain PPMXL proper motions (Roeser et al. 2010) for a 1° square field centered on the targets shown in Figure A3, and then iteratively use the technique of reduced proper motion (Yong & Lambert 2003; Gould & Morgan 2003) to distinguish between giants and dwarfs.

A.3. *Estimated Reference Frame Absolute Parallaxes*

With the spectral classification of the reference stars complete, we combine the $UBVRI$ photometry we have obtained with JHK photometry from 2MASS, to derive the visual extinction to the sources using the reddening relationships from Rieke & Lebofsky (1985). Error bars on the visual extinction are of order 10%. Once determined, we estimate spectroscopic parallaxes using the absolute visual magnitude calibrations for main sequence stars listed in Houket al. (1997), and for giant stars using Cox (2000). These spectroscopic reference star parallaxes are input to our model with errors of 20%. The error bars on the V magnitudes are ± 0.02 mag, and are ± 0.04 mag for the $(B-V)$ colors. Table A4 lists all reference star absolute parallax estimates, spectral types and luminosities.

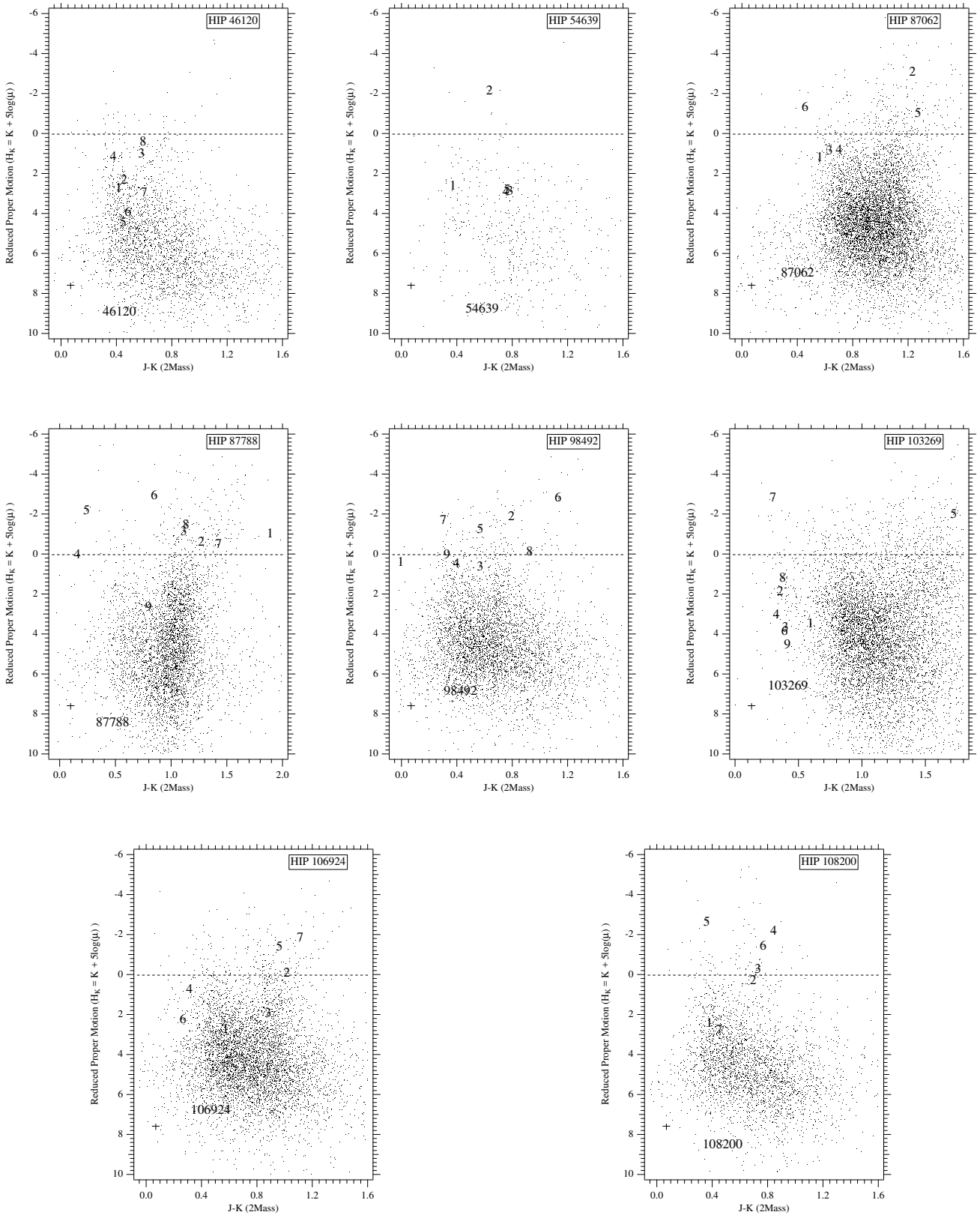

Figure A3. Reduced proper motion diagram for 5800 stars in a 1° field centered on the metal-poor target stars. Star identifications are in Table A3. For a given spectral type, giants and sub-giants have more negative H_K values and are redder than dwarfs in $(J-K)$. H_K values are derived from 'Final' proper motions in Table A6. The small cross at the lower left represents a typical $(J-K)$ error of 0.04 mag and H_K error of 0.17 mag. The horizontal dashed line is a giant-dwarf demarcation derived from a statistical analysis of the Tycho input catalog (Ciardi 2004, private communication).

Table A4. Adopted Spectrophotometric and *HST* Resolved Reference Star Parallaxes

ID	α_{2000}	δ_{2000}	Sp. T.[a]	V	B-V	M_v	A_v	D (pc)	π_{spec} (mas)	π_{HST}[b] (mas)
HIP 46120										
Ref-1	09:24:17.86	−80:36:17.5	G2V	14.34	0.74	4.56	0.37	759	1.317	1.436
Ref-2	09:24:32.59	−80:34:07.1	G5V	13.96	0.81	4.93	0.43	529	1.89	1.550
Ref-3	09:24:13.14	−80:32:58.5	K1V	14.02	1	6.13	0.32	329	3.035	2.355
Ref-4	09:24:09.40	−80:31:59.6	G2V	12.58	0.75	4.56	0.27	353	2.829	2.961
Ref-5	09:24:00.60	−80:31:47.9	G5V	14.76	0.82	4.93	0.38	786	1.273	1.393
Ref-6	09:23:58.95	−80:30:45.2	G7V	13.48	0.89	5.32	0.44	352	2.841	2.664
Ref-7	09:24:57.80	−80:29:29.1	K1V	14.91	1.01	6.13	0.46	463	2.162	2.497
Ref-8	09:24:37.90	−80:28:24.5	K1V	13.21	1.03	6.13	0.43	215	4.66	3.796
HIP 54639										
Ref-1	11:11:02.39	+06:24:15.7	F5V	13.87	0.47	3.34	0.1	1182	0.847	0.843
Ref-2	11:11:19.49	+06:24:20.6	G9III	13.45	0.97	0.8	0.11	3222	0.31	0.309
Ref-3	11:11:04.77	+06:26:39.2	K3V	14.72	1.09	6.75	0	382	2.617	2.408
Ref-4	11:10:57.12	+06:26:37.0	K4V	14.72	1.06	7.12	0	336	2.967	3.812
Ref-5	11:10:43.02	+06:28:16.5	K7V	13.23	1.24	8.23	0	129	9.947	10.306
HIP 87062										
Ref-1	17:47:09.39	−08:45:06.2	F7V	13.36	1.07	3.72	1.89	348	2.876	−[c]
Ref-2	17:47:11.03	−08:44:37.6	K1III	13.32	1.88	0.6	2.65	1009	0.992	−[c]
Ref-3	17:47:16.18	−08:46:17.1	G0V	14.58	1.24	4.2	1.96	490	2.04	2.034
Ref-4	17:47:25.99	−08:45:37.6	G1V	15.67	1.27	4.24	2.3	650	1.541	1.549
Ref-5	17:47:33.27	−08:45:33.7	K2III	14.65	2.02	0.42	3.21	1598	0.626	0.625
Ref-6	17:47:36.10	−08:47:58.0	F0V	13.77	1.05	2.4	2.19	682	1.466	1.467
HIP 87788										
Ref-1	17:56:17.24	−16:25:36.1	Carbon*	14.45	2.35	-.-	-.-	?	?	−[c]
Ref-2	17:56:06.10	−16:23:38.1	K5III	14.57	2.13	-0.2	1.93	3654	0.274	2.530
Ref-3	17:55:58.10	−16:23:24.9	K2III	10.55	1.63	0.42	1.89	454	2.202	1.362
Ref-4	17:56:04.28	−16:24:53.1	A1V	11.98	0.38	1.01	1	982	1.018	1.024
Ref-5	17:56:03.73	−16:26:12.4	A4V	11.04	0.54	1.57	1.01	475	2.105	1.751
Ref-6	17:55:57.02	−16:24:41.2	K1III	11.55	1.39	0.6	1.05	952	1.05	1.138
Ref-7	17:55:50.07	−16:23:33.2	M3III	13.49	2.06	-0.67	1.82	2840	0.353	0.356
Ref-8	17:55:44.75	−16:25:45.0	K5III	13.75	1.85	-0.2	1.09	3625	0.276	0.273
Ref-9	17:55:38.46	−16:23:47.5	G9.5V	13.47	1.3	5.79	1.63	143	7.144	−[c]
Ref-7r	17:55:42.35	−16:23:39.7	K7III	14.41	2.16	-0.3	2.26	3067	0.326	0.325
Ref-8r	17:55:41.08	−16:25:37.2	G1V	13.52	0.88			498	2.007	2.533
HIP 98492										
Ref-1	20:00:49.97	+09:21:57.1	B8V	11.18	0.03	-0.25	0.45	1561	0.641	0.561
Ref-2	20:00:42.85	+09:22:06.7	K2III	11.89	0.7	0.6	0.46	1612	0.621	0.785
Ref-3	20:00:38.94	+09:23:03.4	K1V	14.19	1.01	6.14	0.39	340	2.944	2.331
Ref-4	20:00:33.99	+09:20:44.6	G2V	13.24	0.74	4.56	0.29	473	2.113	2.072
Ref-5	20:00:21.92	+09:22:15.0	*G9III	12.35	1.04	0.8	0.25	1848	0.541	0.571
Ref-6	20:00:17.93	+09:22:01.5	M1III	13.32	1.64	-0.5	0.62	4300	0.233	0.225
Ref-7	20:00:16.45	+09:19:34.6	F5V	13.61	0.57	3.35	0.35	969	1.032	1.050
Ref-8	20:00:18.57	+09:19:30.5	K3III	13.71	1.44	0.24	0.6	3688	0.271	0.270
Ref-9	20:00:14.28	+09:21:22.6	G1V	14	0.7	4.24	0.19	786	1.274	1.308
HIP 103269										
Ref-1	20:55:27.7	+42:22:08.2	K1V	13.04	0.99	6.14	0.44	198	5.065	5.888
Ref-2	20:55:34.9	+42:19:43.8	G1V	12.37	0.65	4.24	0.19	377	2.654	1.259
Ref-3	20:55:31.7	+42:19:40.5	G2V	14.64	0.8	4.56	0.51	823	1.214	1.354

Table A4 continued on next page

Table A4 *(continued)*

ID	α_{2000}	δ_{2000}	Sp. T.[a]	V	B-V	M_v	A_v	D (pc)	π_{spec} (mas)	π_{HST}[b] (mas)
Ref-4	20:55:22.3	+42:18:44.0	G1V	13.36	0.67	4.24	0.13	610	1.642	1.536
Ref-5	20:55:16.3	+42:19:25.4	M1III	15.46	2.61	-0.5	4.14	2312	0.432	0.431
Ref-6	20:55:10.7	+42:19:39.4	G2V	14.14	0.82	4.56	0.5	670	1.494	1.654
Ref-7	20:55:09.4	+42:19:10.5	F5V	11.59	0.55	3.35	0.29	397	2.523	2.564
Ref-8	20:55:06.3	+42:19:15.1	G2V	12.77	0.72	4.56	0.19	398	2.516	0.978
Ref-9	20:55:10.7	+42:17:24.4	G5V	13.49	0.77	4.93	0.23	469	2.134	2.517
HIP 106924										
Ref-1	21:39:26.9	+60:19:20.1	G2V	14.64	1.06	4.56	1.4	544	1.838	1.924
Ref-2	21:39:38.7	+60:17:29.6	K2III	13.25	1.64	0.42	1.64	1738	0.575	0.573
Ref-3	21:39:23.0	+60:17:17.7	K0III	14.73	1.54	0.7	1.7	2867	0.349	0.345
Ref-4	21:39:17.8	+60:17:21.4	F0V	14.3	0.76	2.4	1.41	1261	0.793	0.795
Ref-5	21:39:14.3	+60:16:39.5	K2III	14.63	1.61	0.42	1.41	3670	0.273	0.272
Ref-6	21:39:19.8	+60:15:34.0	F5V	11.44	0.56	3.35	0.21	379	2.636	3.025
Ref-7	21:39:03.8	+60:15:58.0	K2III	14.1	1.8	0.42	2.13	2044	0.489	0.489
HIP 108200										
Ref-1	21:55:43.1	+32:39:08.1	G5V	13.06	0.69	4.93	0.05	414	2.416	2.623
Ref-2	21:55:39.2	+32:38:28.0	K0III	13.65	1.15	0.7	0.44	3159	0.317	0.316
Ref-3	21:55:14.0	+32:37:24.9	K0III	11.15	1.17	0.7	0.58	953	1.05	0.988
Ref-4	21:55:03.0	+32:36:27.4	K2III	12.18	1.3	0.42	0.59	1729	0.578	0.589
Ref-5	21:54:53.4	+32:35:42.7	G0V	13.18	0.65	4.2	0.15	584	1.711	–[c]
Ref-6	21:55:05.4	+32:38:34.5	K2III	13.89	1.25	0.42	0.29	4367	0.229	0.229
Ref-7	21:55:19.1	+32:37:41.3	F8V	15.29	0.67	3.87	0.58	1496	0.669	0.668

[a] Spectral types and luminosity class estimated from colors and reduced proper motion diagram.

[b] The *HST* reference star parallaxes use spectroscopic priors and are not independent.

[c] Reference star not included in model

Two objects in Table A4 warrant mention. Ref-08 for HIP46120 has very weak metal lines, and appears to have a low metallicity. The photometry and spectral continuum are consistent with the temperature of an early K dwarf. HIP87788 Ref-01 appears to be a J-type carbon star.

A.4. *Estimated Reference Frame Proper Motions*

As priors, we test proper motion values when available from the SPM4 (Girard et al. 2011), URAT1(Finch & Zacharias 2016), or the PPMXL (Roeser et al. 2010) catalogs as observations with error in the model. The SPM4 catalog was only available for the HIP 46120 field, while the HIP 87788 and HIP 108200 fields did not have URAT1 values available. The catalogs used for input proper motions are listed in Table A5. The input catalog proper motions and our final *HST* model values are found in Table A6.

Table A5. Astrometric Reference Star Proper Motion Input Catalogs

Target	Catalog
HIP 46120	SPM4
HIP 54639	URAT
HIP 87062	URAT
HIP 87788	PPMXL[a]

Table A5 continued on next page

Table A5 *(continued)*

Target	Catalog
HIP 98492	URAT
HIP 103269	URAT
HIP 106924	URAT
HIP 108200	PPMXL[a]

[a] URAT catalog does not contain this reference frame

Table A6. Astrometric Reference Star Proper Motions

	Input		Final (*HST*)			
ID	μ_α [a]	μ_δ [a]	μ_α	σ_{μ_α}	μ_δ	σ_{μ_α}
HIP 46120						
Ref-1	2.6	-2.18	2.190	0.218	-0.054	0.253
Ref-2	0.36	-6.48	2.860	0.220	-7.039	0.245
Ref-3	-9.44	-0.64	-11.918	0.175	0.740	0.195
Ref-4	-4.16	3.2	-5.831	0.199	-2.828	0.209
Ref-5	-15.48	15.76	-12.927	0.252	15.989	0.280
Ref-6	-36.28	16.28	-35.213	0.258	19.854	0.249
Ref-7	-3.94	-2.16	-4.655	0.319	-1.065	0.321
Ref-8	-4.16	3.2	-4.013	0.211	3.332	0.209
HIP 54639						
Ref-1	-11	2	-11.627	0.181	1.457	0.158
Ref-2	-19.7	-3.5	-17.837	0.143	-1.330	0.169
Ref-3	-1.7	-5.8	-4.135	0.194	-6.577	0.214
Ref-4	-16	-8.3	-15.605	0.199	-12.139	0.200
Ref-5	-3.4	-38.2	-2.083	0.153	-35.581	0.161
HIP 87062						
Ref-3	1.4	-2.8	1.463	0.145	-2.991	0.163
Ref-4	-1.5	-3.4	-1.645	0.323	-2.895	0.258
Ref-5	-8.9	-6.9	-8.761	0.141	-7.232	0.132
Ref-6	-0.1	-3.6	-0.162	0.149	-3.556	0.129
HIP 87788						
Ref-2	-4.5	1.9	-4.640	0.233	0.373	0.217
Ref-3	-19.3	-28.6	-20.319	0.109	-30.225	0.111
Ref-4	-5.6	3.4	-4.310	0.138	2.854	0.149
Ref-5	-2.5	3.6	-5.158	0.100	7.424	0.110
Ref-6	-6.4	-0.9	-4.611	0.121	-0.107	0.107
Ref-7	-2.1	-14.4	-3.955	0.627	-8.168	0.841
Ref-8	-4	7.1	-2.892	1.012	-8.544	0.730
Ref-101	-4.6	-8.8	-3.084	0.248	-4.772	0.216
Ref-102	3.9	-0.3	3.352	0.143	-5.042	0.168
HIP 98492						
Ref-1	7.8	7.7	10.411	0.139	6.070	0.129
Ref-2	5.9	2.3	2.638	0.171	2.327	0.199
Ref-3	-4.5	-3.8	-7.883	0.260	-3.574	0.243
Ref-4	5.8	8.4	10.563	0.197	3.334	0.199
Ref-5	4.4	7.9	2.180	0.296	11.309	0.289

Table A6 continued on next page

Table A6 *(continued)*

ID	Input μ_α [a]	Input μ_δ [a]	Final (*HST*) μ_α	σ_{μ_α}	μ_δ	σ_{μ_α}
Ref-6	-2.3	-4.7	-3.765	0.166	-2.458	0.186
Ref-7	3.9	-3	5.721	0.218	-1.275	0.266
Ref-8	2	-6.3	6.457	0.161	-6.758	0.180
Ref-9	-2.4	-0.7	-3.868	0.322	-2.408	0.400
HIP 103269						
Ref-1	-7.6	-26.4	-9.340	0.203	-27.285	0.186
Ref-2	23.5	4.5	26.538	0.197	4.983	0.206
Ref-3	5	-2	3.882	0.334	-3.574	0.367
Ref-4	-7.3	-10.8	-7.860	0.236	-8.644	0.238
Ref-5	-1.8	-7.1	-1.910	0.335	-4.605	0.314
Ref-6	-13.2	-7.5	-10.666	0.324	-8.810	0.331
Ref-7	0.7	6.1	0.111	0.197	8.271	0.193
Ref-8	-9.2	-8.3	-8.570	0.256	-9.039	0.264
Ref-9	-27.8	-12.4	-29.631	0.266	-15.317	0.301
HIP 106924						
Ref-1	-11	-20.3	-11.413	0.168	-18.489	0.176
Ref-2	3.6	-8.9	2.351	0.145	-8.225	0.157
Ref-3	-7.2	-6.6	-5.027	0.192	-8.631	0.228
Ref-4	-5	-1.9	-3.750	0.150	-5.008	0.160
Ref-5	-1.4	1	-1.473	0.175	-0.265	0.184
Ref-6	20.3	12.7	20.795	0.092	13.156	0.103
Ref-7	-6.5	-4.1	-8.683	0.209	-0.730	0.226
HIP 108200						
Ref-1	-0.8	-16.1	-0.316	0.175	-18.600	0.185
Ref-2	-2	-7.4	-2.630	0.199	-4.581	0.171
Ref-3	-11.2	-15.8	-10.469	0.104	-17.051	0.116
Ref-4	9.5	2.6	9.442	0.161	2.615	0.166
Ref-6	-2.4	-2.4	-2.542	0.244	-1.950	0.261
Ref-7	-6.6	-3.5	-7.836	0.476	-1.338	0.445

[a] Spectral types and luminosity class estimated from colors and reduced proper motion diagram.

A.5. *Astrometric Reference Frame Residual Assessment*

Without the target stars, the reference frame stars are modeled many times to assess various plate models, spectrophotometric parallaxes, catalog proper motions, and general stability as a reference star. We graphed reference frame x and y residuals against a number of spacecraft, instrumental, and astronomical parameters. These included x, and y position, radial distance from the center of the field-of-view, V magnitude and B - V color of the reference stars, and time of observation. We see no trends indicating systematic instrumental effects, except for the expected small upward trend in residuals with the faintest star.

A.6. *Astrometric Catalog Residual Assessment*

HST FGS1r has raw distortions of more than an arcsecond, but the OFAD (McArthur et al. 2002) calibration reduces these distortions to around 1 mas in the center of the pickle and below 2 mas over much of the FGS 1r field. The goodness of fit is shown in the table of the astrometric residuals statistics (Table A7) which lists the average position errors and median average deviations of the positions

Table A7. Metal-Poor Target Star Field Quality

ID	Number of Residuals	RMS (mas)	Xres (mas)	Yres (mas)
HIP 46120	351	1.370	1.198	1.225
HIP 54639	322	1.366	1.261	1.252
HIP 87062	256	1.133	0.944	1.183
HIP 87788	267	1.379	1.122	1.287
HIP 98492	353	1.366	1.330	1.172
HIP103269	324	1.194	1.294	0.808
HIP106924	370	1.144	1.116	0.963
HIP108200	295	0.927	0.95	0.907

A.7. *Astrometric Catalog*

The astrometric catalogs from the combined modeling are shown in Table A8

Table A8. Astrometric Catalogs of Metal Poor Target and Reference Stars

Star	Mag[a] V	R.A.[b] deg	Dec.[b] deg	ξ[c] arcsec	σ_ξ arcsec	η[c] arcsec	σ_η arcsec
HIP 46120	10.14	141.09068	-80.51926	-1.03559	0.00013	730.34794	0.00014
Ref-1	14.42	141.07442	-80.60486	306.77912	0.00024	748.33586	0.00022
Ref-2	14.02	141.13579	-80.56864	173.78383	0.00020	772.70577	0.00021
Ref-3	14.09	141.05475	-80.54958	109.62841	0.00021	718.73084	0.00023
Ref-4	12.63	141.03917	-80.53322	51.75303	0.00022	704.40134	0.00023
Ref-5	14.81	141.0025	-80.52997	41.97647	0.00026	681.61466	0.00026
Ref-6	13.53	140.99562	-80.51256	-20.36440	0.00030	671.44051	0.00030
Ref-7	14.96	141.24083	-80.49142	-108.58955	0.00035	810.34446	0.00039
Ref-8	13.28	141.15792	-80.47347	-168.80552	0.00023	755.47584	0.00022
HIP 54639	11.38	167.74858	6.41859	-0.93955	0.00011	675.41028	0.00011
Ref-1	13.85	167.75996	6.40436	56.67655	0.00018	644.87230	0.00018
Ref-2	13.47	167.83121	6.40572	290.49465	0.00018	749.24212	0.00019
Ref-3	14.71	167.76988	6.44422	34.36981	0.00025	790.93086	0.00026
Ref-4	14.73	167.738	6.44361	-70.07244	0.00022	744.85367	0.00023
Ref-5	13.24	167.67925	6.47125	-302.26219	0.00019	755.48500	0.00020
HIP87062							
Ref-1	10.59	266.8672	-8.78091	199.16810	0.00011	675.88272	0.00010
Ref-2	13.37	266.78913	-8.75172	-80.40516	0.00025	775.29420	0.00027
Ref-3	13.3	266.79596	-8.74378	-56.82072	0.00019	804.55110	0.00018
Ref-4	14.57	266.81742	-8.77142	21.57447	0.00020	705.92984	0.00019
Ref-5	15.62	266.85829	-8.76044	166.15922	0.00045	748.87200	0.00029
Ref-6	14.58	266.88862	-8.75936	273.67705	0.00017	754.89600	0.00016
HIP87788	11.32	268.99363	-16.41082	-0.91890	0.00012	710.27933	0.00014
Ref-2	14.46	269.02542	-16.39392	-109.37292	0.00033	649.80905	0.00031
Ref-3	10.56	268.99208	-16.39025	4.55778	0.00018	637.04227	0.00018
Ref-4	11.89	269.01783	-16.41475	-84.63560	0.00020	724.71871	0.00021
Ref-5	10.99	269.01554	-16.43678	-76.76387	0.00017	803.91410	0.00018
Ref-6	11.56	268.98758	-16.41144	19.99242	0.00018	712.94625	0.00017
Ref-7	13.48	268.95862	-16.39256	119.64677	0.00043	646.17077	0.00045
Ref-8	13.87	268.93646	-16.42917	196.56365	0.00046	776.87247	0.00041
Ref-101	14.41	268.92646	-16.39436	231.08096	0.00049	652.13340	0.00043

Table A8 continued on next page

Table A8 *(continued)*

Star	Mag[a] V	R.A.[b] deg	Dec.[b] deg	ξ[c] arcsec	σ_ξ arcsec	η[c] arcsec	σ_η arcsec
Ref-102	13.52	268.92117	-16.427	248.61500	0.00028	769.72135	0.00033
HIP 98492	11.58	300.13994	9.353	-1.04389	0.00013	690.42745	0.00013
Ref-1	11.13	300.20821	9.36586	245.71686	0.00015	694.40018	0.00015
Ref-2	11.92	300.17854	9.36853	143.56687	0.00021	721.97302	0.00021
Ref-3	14.19	300.16225	9.38428	96.06615	0.00032	787.67128	0.00031
Ref-4	13.24	300.14162	9.34572	0.35508	0.00021	663.61701	0.00022
Ref-5	12.36	300.09133	9.37083	-160.11894	0.00036	783.23070	0.00034
Ref-6	13.3	300.07471	9.36708	-220.85237	0.00021	780.01338	0.00022
Ref-7	13.59	300.06854	9.32628	-267.59091	0.00025	639.16527	0.00031
Ref-8	13.69	300.07738	9.32514	-237.36517	0.00019	629.58129	0.00021
Ref-9	14	300.0595	9.35628	-280.58999	0.00036	750.99604	0.00038
HIP 103269	10.3	313.82004	42.29906	-1.06961	0.00010	765.31094	0.00010
Ref-1	13.07	313.86533	42.36894	-235.75461	0.00018	615.48889	0.00017
Ref-2	12.39	313.89562	42.32883	-228.81074	0.00020	780.62742	0.00018
Ref-3	14.66	313.88225	42.32792	-196.45390	0.00033	764.52578	0.00031
Ref-4	13.4	313.843	42.31222	-77.67290	0.00021	757.33490	0.00021
Ref-5	15.29	313.81775	42.32372	-42.60106	0.00031	686.87482	0.00031
Ref-6	14.18	313.79475	42.32761	2.27333	0.00030	642.63245	0.00030
Ref-7	11.63	313.78933	42.31958	29.19090	0.00016	659.34975	0.00017
Ref-8	12.83	313.77604	42.32086	57.13444	0.00024	636.81119	0.00022
Ref-9	13.54	313.79454	42.29011	74.22246	0.00025	756.71502	0.00025
HIP 106924	10.37	324.81503	60.28452	-0.74170	0.00010	680.29568	0.00009
Ref-1	14.67	324.86208	60.32225	-158.70460	0.00019	701.12039	0.00019
Ref-2	13.28	324.91125	60.29156	-93.96140	0.00018	826.50046	0.00015
Ref-3	14.75	324.84567	60.28825	-34.83180	0.00024	724.59364	0.00022
Ref-4	14.32	324.82433	60.28928	-23.04487	0.00017	688.31047	0.00016
Ref-5	14.65	324.80954	60.27764	25.94452	0.00021	681.24496	0.00020
Ref-6	11.49	324.83242	60.25944	68.67841	0.00010	745.75221	0.00009
Ref-7	14.14	324.766	60.26611	95.59408	0.00022	627.50410	0.00021
HIP 108200	11.01	328.8199	32.64515	29.01044	0.00008	660.57750	0.00008
Ref-1	13.08	328.9295	32.65225	-292.13097	0.00016	749.66380	0.00016
Ref-2	13.68	328.91312	32.64111	-231.76706	0.00017	770.29653	0.00015
Ref-3	11.21	328.80829	32.62358	88.71493	0.00010	721.85232	0.00010
Ref-4	12.26	328.76229	32.60761	239.24013	0.00016	728.26817	0.00015
Ref-6	13.94	328.77263	32.64292	166.52997	0.00023	619.34112	0.00022
Ref-7	15.26	328.8295	32.62814	22.67684	0.00041	728.01902	0.00033

[a] V mag calculated from Hubble Photometry

[b] Predicted coordinates for equinox J2000.0

[c] Relative coordinates in the reference frame of the constrained plate .

REFERENCES

Adelberger, E.G., et al. 1998, Rev. Modern Physics 70, 1265
Adelberger, E.G., et al. 2011, Rev. Modern Physics 93, 195
Angulo, C., et al. 1999, Nuc Phys A, 656, 3
Benedict, G. F., McArthur, B. E., Feast, M. W., Barnes, T. G., Harrison, T. E., Patterson, R. J., Menzies, J. W., Bean, J. L., Freedman, W. L. 2007, AJ, 133, 1810
Benedict, G.F. et al. 2011, AJ, 142, 187
Bessel, M.S. 1990, A&AS, 83, 357
Bessell, M. S., Brett, J. M. 1988, PASP, 100, 1134
Bjork, S. R. & Chaboyer, B. 2006, ApJ, 641, 1102
Bonaca, A. et al. 2012, ApJL, 755, 12
Canuto, V. 1970, ApJ, 159, 641
Carney, B.W. & Latham, D.W. 1987, AJ, 92, 116
Carney, B.W., Latham, D.W., Laird, J.B. & Aguilar, L.A. 1994, AJ, 107, 2240
Carpenter, J. M. 2001, AJ, 121, 2851
Carretta, E., Gratton, R. G., Clementini, G., & Fusi Pecci, F. 2000, ApJ, 533, 215
Carretta, E., Bragaglia, A., Gratton, R. G., D'Orazi, V., & Lucatello, S. A&A, 508, 695
Chaboyer, B., Demarque, P., Kernan, P. J., et al. 1996 MNRAS, 283, 683
Chaboyer, B., Demarque, P, Kernan, P.J. & Kraus, L.M. 1998, ApJ, 494 96
Chaboyer, B., & Krauss, L.M. 2002, ApJL, 567, L45
Chakraborty, S., deBoer, R., Mukherjee, A., & Roy, S. 2015, PhyRevC 91, 045801
Cox, A. N. 2000, "Allen's Astrophysical Quantities", (AIP Press: New York)
Creevey, O.L. et al. 2015, A&A, 575, 26
deBoer, R.J. Görres, J., Smith, K., Uberseder, E., Wiescher, M., Kontos, A., Imbriani, G., Di Leva, A., & Strieder, F. 2014, PhyRevC, 90, 035804
Dotter, A., Chaboyer, B., Jevremovic, D., Kostov, V., Baron, E., Ferguson, J. W. 2008 ApJS, 178, 89
Dotter, A., Sarajedini, A., Anderson, J., et al. 2010, ApJ, 708, 698
Dutra, C. M. & Bica, E. 2000, A&A, 359, 347
Eddington, A.S. 1926 The Internal Constitution of the Stars (1988 printing; Cambridge: Cambridge UP), p. 322
Ferguson, J. W., Alexander, D. R., Allard, F., Barman, T., Bodnarik, J. G., Hauschildt, P. H., Heffner-Wong, A., & Tamanai, A. 2005, ApJ, 623, 585
Finch, C. & Zacharias, N. 2016, AJ, in press
Gaia Collaboration et al. 2016, doi:10.1051/0004-6361/201629272 ; arXiv:1609.04153
Girard, T. M., van Altena, W. F., Zacharias, N., Vieira, K., Casetti-Dinescu, D. I., Castillo, D., Herrera, D.,Lee, Y. S., Beers, T. C., Monet, D. G. & López, C. E. 2011, AJ, 142, 15
Gould, A. & Morgan, C. W. 2003, ApJ, 585, 1086
Gratton, R. G., et al. 1997, ApJ, 491, 749
Gratton, R.G., Bragaglia, A., Carretta, E., Clementini, G., Desidera, S., Grundahl, F. & Lucatello, S. 2003, A&A, 408, 529
Gratton, R.G., Carreta, E. & Bragaglia, A. 2012, A&AR, 20, 50
Grundahl, F., Stetson, P. B., & Andersen, M. I. 2002, A&A, 395, 481
Haft, M., Raffelt, G., & Weiss, A. 1994, ApJ, 425, 222
Harris, W. E. 1996, AJ, 112, 1487 (2010 edition)
Harrison, T. E., Bornak, J., McArthur, B. E., & Benedict, G. F. 2013, ApJ, 767,7
Hauschildt, P. H., Allard, F., & Baron, E. 1999, ApJ, 512, 377
Houk, N., Swift, C. M., Murray, C. A., Penston, M. J., & Binney, J. J. 1997, in Proc. ESA Symposium on Hipparcos—Venice, ed. M. A. C. Perryman & P. L. Bernacca (1997 ESA SP-402; Noordwijk: ESA), 279
Hubbard, W. B., & Lampe, M. 1969, ApJS, 18, 297
Holtzman, J. A. 2010, Advances in Astronomy, 2010, article id. 193086
Iglesias, C. A., & Rogers, F. J. 1996, ApJ, 464, 943
Jefferys, W. H., Fitzpatrick, M. J., & McArthur, B. E. 1988, Celestial Mechanics 41, 39
Krishna Swamy, K.S. 1966, ApJ, 145 174
Lindegren, L., et al. 2017, doi:10.1051/0004-6361/201628714 ; arXiv:1609.04303
Lutz, T.E. & Kelker, D.H. 1973, PASP, 85, 573
McArthur, B., Benedict, G. F., Jefferys, W. H., & Nelan, E. 2002, The 2002 HST Calibration Workshop : Hubble after the Installation of the ACS , the NICMOS Cooling System, 373
McArthur, B. E., Benedict, G. F., Jefferys, W. H., & Nelan, E. 2006, The 2005 HST Calibration Workshop: Hubble After the Transition to Two-Gyro Mode, 396
McArthur, B. E., Benedict, G. F., Barnes, R., Martioli, E., Korzennik, S., Nelan, E., & Butler, R. P. 2010 ApJ715, 1203
McArthur, B., Benedict, G. F., Jefferys, W. H., & Nelan, E. 1997, The 1997 HST Calibration Workshop with a New Generation of Instruments, 472
Michalik, D., Lindegren, L. & Hobbs, D. 2015, A&A, 574, A115
Milone, A.P. 2015, MNRAS, 445, 1672
Milone, A. P., Marino, A. F., Piotto, G., et al. 2012a, ApJ, 745, 27
Milone, A. P., Piotto, G., Bedin, L. R., et al. 2012b, ApJ, 744, 58
Milone, A. P., Marino, A. F., Piotto, G., et al. 2013, ApJ, 767, 120
Milone, A. P., Marino, A. F., Piotto, G., et al. 2015a, MNRAS, 447, 927
Milone, A. P., Marino, A. F., Piotto, G., et al. 2015b, ApJ, 808, 51
Milone, A. P., Piotto, G., Renzini, A., et al. 2016, MNRAS,
Nelan, E. P. 2007, Fine Guidance Sensor instrument Handbook, 16
O'Malley, E. O., McWilliam, A., Chaboyer, B. ApJ, submitted
Perryman, M.A.C., & ESA 1997, The HIPPARCOS and TYCHO catalogues. Astrometric and photometric star catalogues derived from the ESA HIPPARCOS Space Astrometry Mission, ESA SP, 1200
Piotto, G. 2009, IAUS, 258, 233
Piotto, G. et al. 2015, AJ, 149, 91
Planck Colloaboration XVI 2014, 571, A16
Pont, F., Mayor, M., Turon, C., & VandenBerg, D. A. 1998, A&A, 329, 87
R Development Core Team (2005). R: A language and environment for statistical computing, R Foundation for Statistical Computing, Vienna, Austria. ISBN 3-900051-07-0, URL
Reid, I. N. 1997, AJ, 114, 161
Rieke, G. H., Lebofsky, M. J. 1985, ApJ, 288, 618
Roeser, S., Demleitner, M., & Schilbach, E. 2010, AJ, 139 2440
Sarajedini, A., Bedin, L. R., Chaboyer, B., et al. 2007, AJ, 133, 1658
Schlegel, D. J., Finkbeiner, D. P., & Davis, M. 1998, ApJ, 500, 525
Schuster, W.J., Moitinho, A., Márquez, A., Parrao, L., & Covarrubias, E. 2006, A&A, 445, 939
Silva, J.S, Schuster, W.J. & Contreras, M. E. 2012, RMxAA, 48, 109
Sirianni, M., Jee, M. J., Benítez, N., et al. 2005, PASP, 117, 1049
Soderblom, D. R., Nelan, E., Benedict, G. F., McArthur, B., Ramirez, I., Spiesman, W., & Jones, B. F. 2005, AJ, 129, 1616
Standish, Jr., E. M. 1990, A&A, 233, 252
Stassun, K.G. & Torres, G. 2016, ApJL, 831, 6

Tanner, J.D., Basu, S. & Demarque, P. 2014, ApJL, 785, 13
Thoul, A. A., Bahcall, J. N., & Loeb, A. 1994, ApJ, 421, 828
van Altena, W. F., Lee, J. T., &Hoffleit, E. D. 1995 The General Catalogue of Trigonometric [Stellar] Parallaxes, New Haven, CT: Yale University Observatory 4th ed. (YPC95)
VandenBerg, D. A. & Clem, J. L. 2003, ApJ, 126, 778
VandenBerg, D. A., Bergbusch, P. A., Dotter, A., et al. 2012, ApJ, 755, 15
VandenBerg, D. A., Brogaard, K., Leaman, R., et al. 2013, ApJ, 775, 134
van Leeuwen, F. 2007, HIPPARCOS, The New Reduction of the Raw Data, Astrophys. Space Sci. Lib. (Springer), 350
Watkins, L.L., van der Marel, R.P., Bellini, A. & Anderson, J. 2015, ApJ, 812, 149
Xu, Y., Takahashi, K., Goriely, S., Arnould, M., Ohta, M. & Utsunomiya, H. 2013, Nuclear Phys A, 918 61 (NACRE II)
Yamashita, Y., Nariai, K., & Normoto, Y. 1978, "An Atlas of Representative Stellar Spectra", (Halsted Press: New York)
Yong, D., Lambert, D. L. 2003, PASP, 115 796